UNIVERSITY OF CALIFORNIA
RIVERSIDE

Measurement of the Higgs Boson Properties at $\sqrt{s} = 13$TeV With CMS in the $\gamma\gamma$ Decay Channel

A Dissertation submitted in partial satisfaction
of the requirements for the degree of

Doctor of Philosophy

in

Physics

by

Manuel Alejandro Olmedo

September 2017

Dissertation Committee:

Professor Gail Hanson, Chairperson
Professor Owen Long
Professor Haibo Yu

The Dissertation of Manuel Alejandro Olmedo is approved:

Committee Chairperson

University of California, Riverside

Acknowledgments

To my family: Juana Negrete Garcia (Mother), Mario Olmedo Flores (Father), Mario Jesus Olmedo Negrete (Brother) and his new family, Jeiying Kong (Sister in law) and Luna Aurelia Olmedo-Kong (Niece). Gracias por siempre estar a mi lado en las buenas y en las malas, y mas que nada por el pozole y el menudo. To CERN people: I would like to thank Chris Palmer for being the first helping hand in 2013. Rachel Yohay for being a pixel mentor and a career developer, Camilo Andres Carrillo Montoya for our exiting and fruitful collaboration in early 2014, and Matthias Webber for being the only physics mentor I had at CERN. Finally I would like to thank my advisor Gail Hanson, in 2012 she took me in as a graduate student with unhindered support, while we went through real tough times and our situation was non-ideal, we managed to break through and come out fightig.

ABSTRACT OF THE DISSERTATION

Measurement of the Higgs Boson Properties at $\sqrt{s} = 13$TeV With CMS in the $\gamma\gamma$ Decay Channel

by

Manuel Alejandro Olmedo

Doctor of Philosophy, Graduate Program in Physics
University of California, Riverside, September 2017
Professor Gail Hanson, Chairperson

The decay of the Higgs boson to two photons is one of the major analysis channels for Higgs physics studied at the LHC. Together with the four-lepton decay channel, it provided the most statistically robust signal leading to the Higgs discovery in 2012. Although the particle has been extensively studied at 7 TeV and 8 TeV, research into higher collision energies (13 TeV) is necessary for further characterization. The two-photon collaboration in CMS has developed analysis tools to investigate these high-energy collision events. Important results are a measured signal strength of $\sigma_{obs}/\sigma_{theoretical} = 1.16^{+0.11}_{-0.10}$ and a measured mass of m_H=125.09 GeV with 9.3σ significance.

Contents

List of Figures

List of Tables

Chapter 1

Introduction

In 1964 Peter Higgs, Franiçois Englert, Robert Brout, Gerald Guralnik, Carl Hagen and Tom Kibble all wrote a set of papers that revolutionized our understanding of particle physics. The puzzle of giving mass to the vector bosons while preserving gauge invariance was solved by this work using the concept of symmetry breaking. It took 48 years for their predictions to be proven as real physical phenomena. This work was done at the Center for European Nuclear Research (CERN) using the Large Hadron Collider (LHC) and the Compact Muon Solenoid (CMS) and A Toroidal LHC ApparatuS (ATLAS) experiments [6] [3]. My work was done with the CMS collaboration (which is composed of $\sim$ 3000 scientists) in the $H{\rightarrow}\gamma\gamma$ working group. This decay channel was one of the main contributors for the 2012 discovery of the higgs particle, during that time the LHC ran at an energy of 8 TeV an collected about 20 fb^{-1}. Since then, the LHC has ramped up to a collision energy of 13 TeV and is projected to collect about 5 times more data by the end of 2018.

Chapter 2

The Standard Model

2.1 Brief Description

The standard model of particle physics is the biggest achievement of fundamental particle physics research. It is a robust description of all the fundamental interactions and particles of nature. The components of the model are leptons, quarks, and the gauge bosons that define how the leptons and the quarks interact; these are the photon γ, W and Z boson, gluons g, and the recently discovered Higgs particle H (the graviton has not been experimentally observed). Both the leptons and quarks come in three different flavors (types) which are ordered in increasing mass; the electron is the lightest (first generation), the muon is the second lightest(second generation), and the tau is the most massive lepton (third generation). Each lepton has an associated neutrino, these are the electron, muon, and tau neutrino. In the same fashion the quarks come in three flavors ordered from least to most massive; the up and down quarks are the lightest (first generation), the charm

and strange quarks are the second lightest (second generation), and the top and bottom quarks are the most massive (third generation). The interactions are divided into the electromagnetic interaction, which is mediated by the photon, the weak interaction which is mediated by the W and Z boson, the strong interaction which is mediated by the gluons, and the higgs interaction which is mediated by the higgs particle.

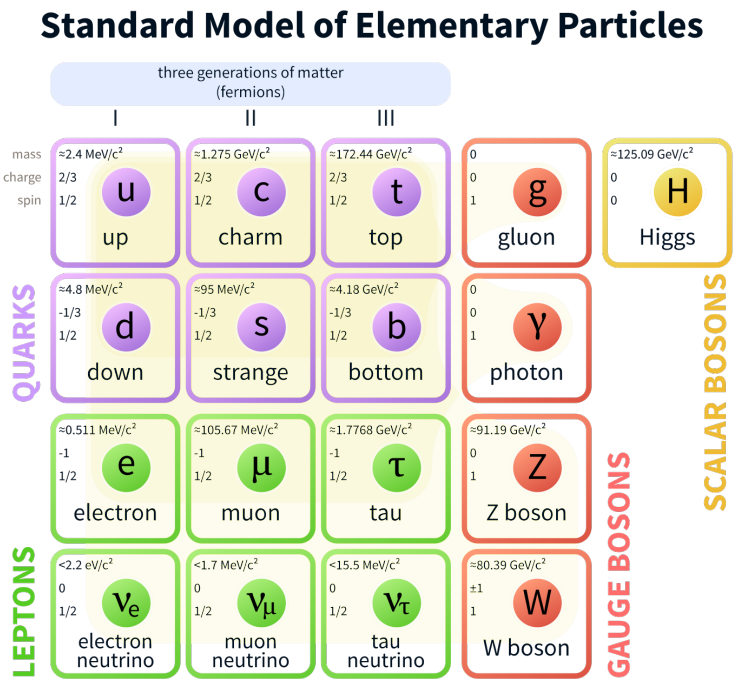

Figure 2.1: The Standard Model Of Particle Physics

2.2 Brief Description Of Mathematical Formulation

The Standard Model (SM) Lagrangina is invariant under the SU(3)×SU(2)×U(1) symmetry group. All matter particles are fermions, which must satisfy the dirac equation:

$$i\gamma^{\mu}\partial_{\mu}\psi \text{ - } m\psi = 0$$

where γ^{μ} are the gamma matrices and $\mu = 0, 1, 2, 3$. The solutions to this equation are 4 component bispinors, this is an object that is composed of two sets of spinors representing the *up* and *down* states of matter and antimatter. In total the SM contains 96 fermionic fields, 3 leptons, 3 neutrinos, 6 quark flavours with 3 possible color charges each. This adds to a total of 24 types, which is double to account for antimatter, and doubled again to account for both *up* and *down* states for a total of 96 components.

For Quantum Electrondynamic (QED) interactions the electromagnetic tensor $F^{\mu\nu}$ $= \partial_{\mu}A_{\nu}$ - $\partial_{\nu}A_{\mu}$ is the source for electromagnetic interactions. The source for the photon is the vector field A_{μ}. This vector field naturally occurs when one demands local gauge invariance under U(1) gauge transformations of a field. The most basic interaction of a photon and a charged fermion is shown in figure 1.2.

The next interaction arises when demanding local gauge invariance under SU(3). This corresponds to Quantum Chromodynamics (QCD) and is mediated by the gluon. In the same fashion there is a gluon field strength given by $G^{a}_{\alpha\beta} = \partial_{\alpha}A^{a}_{\beta}$ - $\partial_{\beta}A^{a}_{\alpha} \mp g_{a}f^{abc}A^{b}_{\alpha}A^{c}_{\beta}$ where a, b, $c = 1, 2, 3, \ldots, 8$ are the color indices and α, $\beta = 0, 1, \ldots, 3$ are the space time

Lepton, neutrinos	Quarks
$\psi_e, \psi_\mu, \psi_\tau$	$\psi^b_u, \psi^b_s, \psi^b_t$
$\psi_{\nu_e}\ \psi_{\nu_\mu}\ \psi_{\nu_\tau}$	$\psi^b_d, \psi^b_c, \psi^b_b$
	$\psi^r_u, \psi^r_s, \psi^r_t$
	$\psi^r_d, \psi^r_c, \psi^r_b$
	$\psi^g_u, \psi^g_s, \psi^g_t$
	$\psi^g_d, \psi^g_c, \psi^g_b$

Table 2.1: Fermionic fields

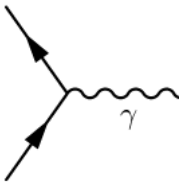

Figure 2.2: Electronmagnetic interaction Feynman diagrams

indices. The main difference between the electromagnetic interaction of QED vs QCD is the self interaction of the gluon. This self interaction is what leads to asymptotic freedom.

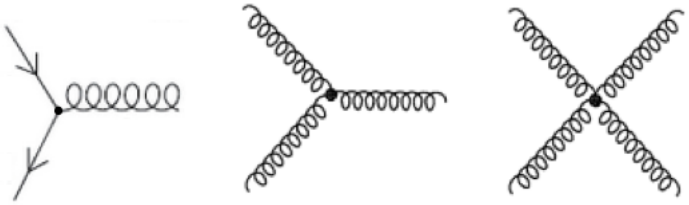

Figure 2.3: Strong interaction Feynman diagrams

The final component in the SM are the Electroweak (EW) interactions. The EW interactions arise when local gauge invariance is demanded for SU(2)×U(1) gauge transformations. This symmetry is evident when writing the ferminoic components of the the lagrangian by it's left handed and right handed components. Pairing the electron with its corresponding neutrino into a spinor yields a new object called a weak isospinor. In the same way there is an approximate strong isospin between the proton and the neutron (you can transform between a proton or neutron), there is weak isospinor for the leptons. The charge associated with this symmetry is called weak hypercharge, its relation to electromagnetic charge is $Q = I_w^3 - \frac{Y_w}{2}$. Where I_w^3 is the weak isospin value, the isospinor has a charge of $\frac{1}{2}$

and it has three states, $I_w^3 = \frac{1}{2}$ corresponding to the neutrino, $I_w^3 = -\frac{1}{2}$ corresponding to a left handed electron, and $I_w^3 = 0$ corresponding to the right handed electron singlet. Y_w is the weak hypercharge, this value is associated with the particles chirality. Left handed particles have $Y_w = -1$ and right handed particles have $Y_w = -2$. This formalism is handled under the SU(2) symmetry. Given the fact that right handed neutrinos have never been observed, there is still a right handed electron singlet. This singlet is invariant under the U(1) symmetry as well and it's conserved current is the weak hypercharge. The same is done with the quarks, but the isospinors are pairs of different flavored quarks, the pairing can be observed in figure 2.1.

2.3 Spontaneous Symmetry Breaking

Once the symmetry that fits these particles has been realized, the next step is to make the lagrangian gauge invariant under local transformations of this type. This would lead to 4 new potentials, three for SU(2) and one for U(1). The next step is to introduce another weak isospin field with $I_w^3 = \frac{1}{2}$ and $Y_w = 1$

$$\phi = \begin{pmatrix} \phi^\dagger \\ \phi^0 \end{pmatrix} = \begin{pmatrix} \frac{1}{\sqrt{2}}(\phi_3 + i\phi_4) \\ \frac{1}{\sqrt{2}}(\phi_1 + i\phi_2) \end{pmatrix}$$

where ϕ_i (i=1,2,3,4) are all real valued fields. Assuming this new weak isospin field interacts with fermions as well, one can write an interaction lagrangian that involves them as well. Of main interest though is how this field affects the propagators that carry the weak current [11].

$$D_\mu\phi = (\partial_\mu - \frac{i}{2}g\tau \cdot W_\mu - \frac{i}{2}g' X_\mu)\phi$$

where W_μ are fields due to SU(2) and X_μ are the fields due to U(1). The field ϕ has a potential term which can be written by

$$m^2(\phi^\dagger\phi) + \lambda(\phi^\dagger\phi)$$

minimizing this potential and allowing m^2 to run negative yields the famous mexican hat potential. To break the symmetry, a perturbation along the the local minimum is done on the field. This yields a new field which can be written as

$$\phi(x) = \begin{pmatrix} 0 \\ \eta + \dfrac{\sigma(x)}{\sqrt{2}} \end{pmatrix}$$

where the idead of local fields is expressed by making them functions of the spacetime coordinates x. When multiplying out the covariant derivative with this new field configuration, one ends up with the following

$$(D_\mu\phi)^\dagger(D_\mu\phi) = \frac{1}{2}(\partial_\mu\sigma)^2 + \frac{g^2\eta^2}{4}((W_\mu^1)^2 + (W_\mu^2)^2) + \frac{\eta^2}{4}(gW_\mu^3 - g'X_\mu)^2 \cdots$$

. It is clear that there are 4 fields W^1,W^2, $Z_\mu = \dfrac{gW_\mu^3 - g'X_\mu}{g^2 + g'^2}$ and a new orthogonal field $A_\mu = \dfrac{g'W_\mu^3 + gX_\mu}{g^2 + g'^2}$. It is clear that this fields correspond to the neutral Z boson, the chraged W bosons and the electromagnetic field A. Therefore the breaking of SU(2)×U(1) symmetry by a gauge invariant scalar field yields the elecroweak sector (higgs terms have been igonored). The manifestation of this scalar field is the higgs boson.

Chapter 3

The Large Hadron Collider

3.1 Accelerator Complex

The LHC is the biggest particle accelertator in the world. It has designed center of mass collision energy of $\sqrt{s}$ = 14 TeV and a circumference of 27 km. The LHC itself though is the last stage in a chain of accelerators that shape and ramp up the beam. At the beginning stage, the Linear Accelerator 2 (LINAC2) [5] raises the energy of the proton bunch to 50 MeV. In the following stage the beam enters the Proton Synchroton Booster (PSB). The PSB consists of four circular accelerators that boost the proton bunches to 1.4 GeV. At the next stage, the Proton Synchroton (PS) raises the energy to 25 GeV. It then enters the the Super Proton Synchroton (SPS) where the proton bunch energy is raised to 450 GeV. Finally the beam enters the LHC. Once in the LHC each beam is ramped up to to an energy of 6.5 TeV each, the two beams move in oposite directions for a nominal $\sqrt{s}$ = 13 TeV.

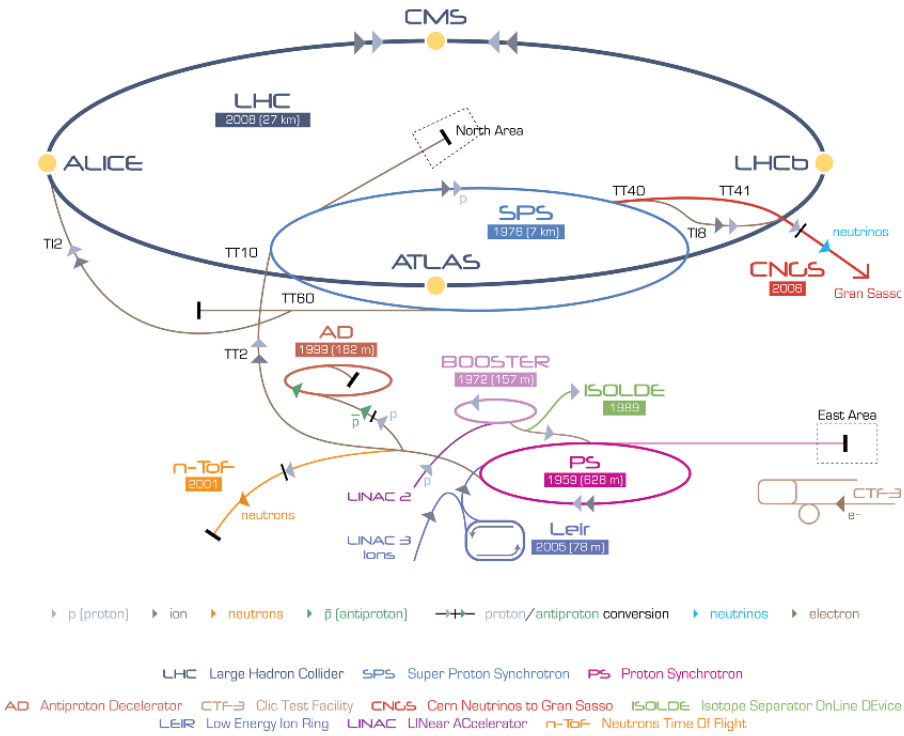

Figure 3.1: LHC injection chain.

3.2 Acceleration

The acceleration at the LHC is provided by 16 Radio Frequency (RF) cavities seperated into two systems with 2 cryostats each (4 cavities per cryostat). The cavities are single cell niobium sputtered copper and are located at IP4 of the LHC, a section of the LHC adjacent to the Compact Muon Solenoid. Each cavity is driven by its own klystron. Each RF system must provide 16 MV in coast, meaning that each cavity can provide 2 MV, at 400 MHz. One turn trough the LHC increases the energy of the beam to 485 keV, which means that it will take about 20 minutes for the beam to ramp up to 6.5 TeV (based on the orbit time of 90μs).

3.3 Magnets

The LHC is composed of 1232 dipole magnets. The dipole magnets provide the steering needed for keeping such an energetic charged beam in circular orbit. Each dipole magnet is 15 meters long and is composed of NbTi wire. They have a field strenght of 8.33 T and carry 11,850 A of current at a beam energy of 6.5 TeV. The magnets are cooled to an operating temperature of 1.9 K.

Chapter 4

The Compact Muon Solenoid (CMS)

4.1 Structure And Design

The CMS detector is composed of 5 main subdetectors: The silicon pixel tracker, the silicon strip tracker, the Electromagnetic Calorimeter (ECAL), the Hadron Calorimeter (HCAL), and the muon chambers. The pixel tracker, strip tracker, ECAL and HCAL are all contained within the super conducting solenoid which provides a uniform magnetic field of 3.8 T. Outside the solenoid the returning magnetic field is stabalized by an iron **return yoke** but its reduced in magnitude. The total size of CMS is 15.0 m in diameter by 21.6 m in length, and it weighs 12,500 tonnes.

4.2 Silicon Pixel

The pixel detector is the first to provide tracking information for charged particles in all of CMS. It's main function is to use its impressive resolution to reconstruct collision vertices; a particle's position in the longitudinal direction can be determined up to a precision of 15 μm. It has a radius of about 10 cm, the barrel spans a length of 54 cm from the origin and the end caps lie at about 34 cm for the inner disk and 46 cm for the outer disk. Its structure is divided into two main parts, the barrel pixel and the forward pixel detector. The barrel pixel provides tracking or hit information from particles having $|\eta|$ <2.5 and it's composed of 3 layers, the forward pixel spans $|\eta|$ >2.5 and is composed of two disks. The sensors are composed of n^+ doped silicon insertions on a p doped silicon substrate. The p-n junction is then integrated to a complex readout chip which is connected through a bump bond. The sensor has the following parameters: The pixel cell is 150 μm $\times$ 150 μm and a thickness of 250μm and has a designed depletion voltage of 250 volts [2].

4.2.1 Charge Sharing

To better determine the position of a particle track charge sharing between pixels is increased as much as possible. Charge sharing is achieved by the displacement of the charge induced by an ionizing particle. As the charge moves down the biasing electric field it drifts to the sides due to the perpendicular magnetic field (Lorentz force). This increases the number of pixels that record a hit and is used to better determine the position of a track [1].

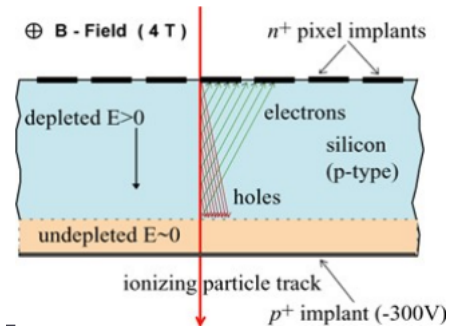

Figure 4.1: Charge sharing between pixels.

4.2.2 Data Acquisition and Readout

The read out of the pixel comes in two levels. The first level is directly done within the integrated circuit next to the pixel sensors. The second level is done externally in the front-end electronics which read out the pixel detector. The pixels sensors are organized in the following way: A single pixel cell consists of pixels organized by double columns, each column is 80 pixels tall and there are 26 double columns for a total of 4,160 pixels. Each double column is connected to a data buffer and time stamp buffer; these buffers hold the data until a trigger decission is sent by the L1 trigger. When a signal is received from an ionizing particle it goes through a shaper and a pre-amplifier; a comparator than compares the amplitude to a threshold setting that is tuned differently for each pixel. If the hit passes the threshold it is then sent to the data buffer, and its time stamp is sent to the time stamp buffer. The sensor is constantly being read out at rate of 40 MHz and stores the data in the buffers for 3.2 μs while waiting for an L1 trigger. If no L1 trigger is received the data and time stamps are erased. If an L1 trigger is recieved, the data (signal amplitude, pixel hit

addresses) is then sent to the front-end. From the data buffer, the data are transfered via optical links to the the Front End Driver (FED) which communicates with the rest of CMS. Before the data is recieved by the FEDs as an optical signal, the electrical signal from the sensors in coverted into optical pulses by the Analog Optohybrid (AOH).

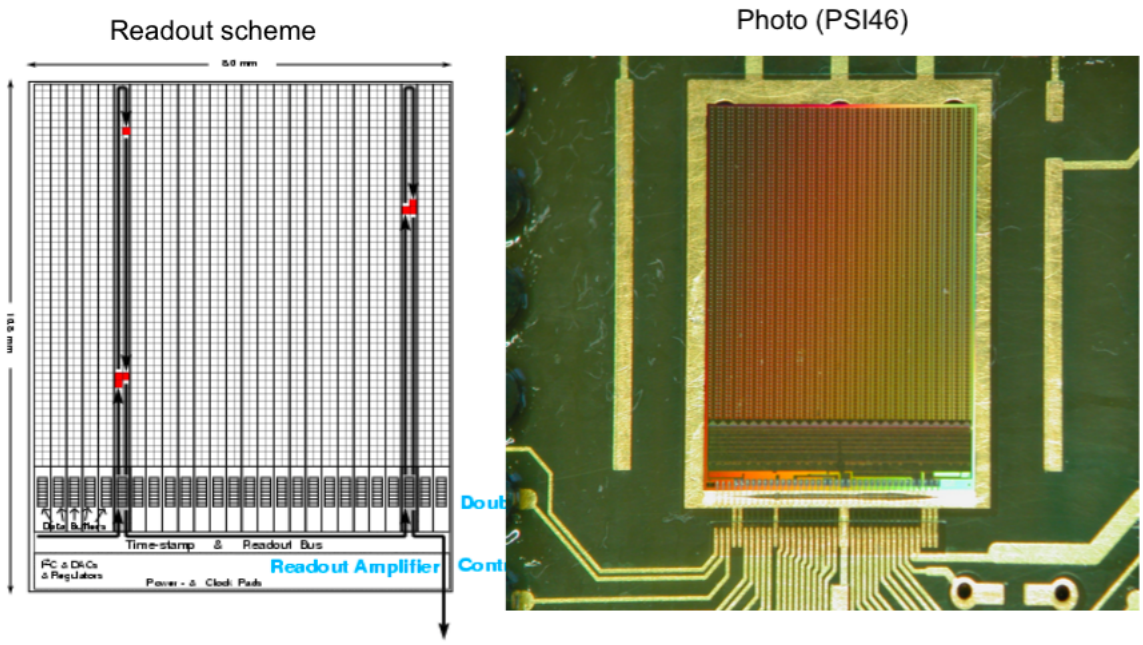

Figure 4.2: Image of a unit of silicon pixels.

4.3 Silicon Strip Tracker

After the pixel layer, the silicon strip tracker is the next tracking layer. The strip tracker is subdivided into the Tracker Inner Barrel (TIB), Tracker Outer Barrel(TOB), Tracker Inner Disk (TID) and the Tracker End Cap (TEC). The fundamental component

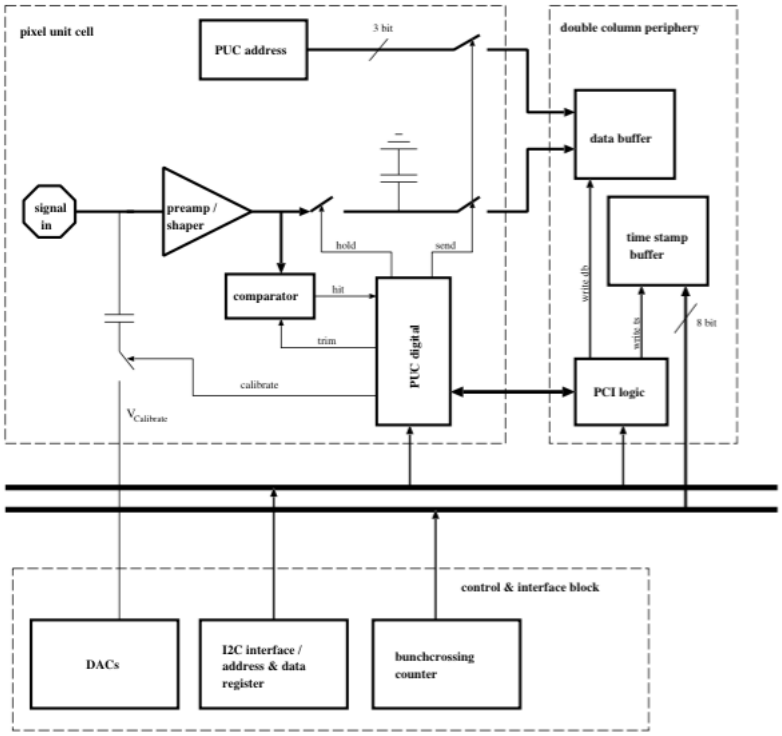

Figure 4.3: Schematic of the single pixel unit.

in each region is the silicon micro-strip. Unlike the pixel detector which has square sensors, the main unit is a strip. A typical strip on average can be 12.5 cm, with the largest strips being 20.0 cm long. The strip tracker holds more general responsobilities than the pixel. Using the pixel detector, the strip tracker has to reconstruct tracks from jets, electrons, muons and other charged particles like pions, it has to determine their p_T with a resolution of $\frac{\Delta p_T}{p_T} = .15\%$ and do this within a 25 ns window.

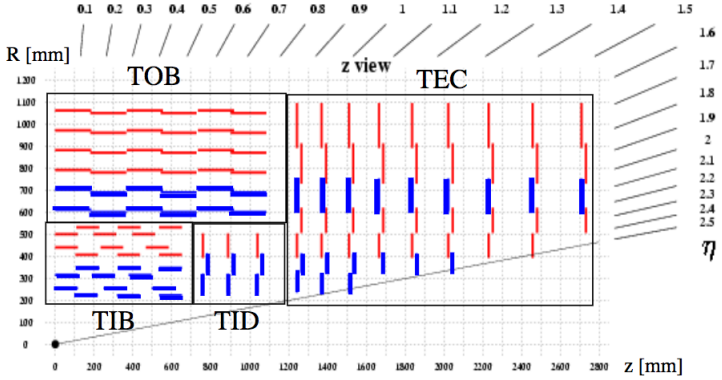

Figure 4.4: Silicon strip tracker geometry.

4.4 The Electromagnetic Calorimeter

The Electromagnetic Calorimeter (ECAL) is responsible for measuring the energy of electrons, photons and other charged particles. Its main unit is a $PbWO_4$ crystal with an Avalanche Photo Diode (APD) in the Barrel (vacuum phototriode nn the endcaps) to measure the scintillation pulse. When a charged particle or a photon hits the crystalthe particle will shower. A shower is produced when the particle undergoes bremstrahlung within the crystal. The emmitted photons will have enough energy to pair produce and the produced particles will again emmit photons, this photons in turn will have enough energy to pair produce and so on. The energy deposited into the crystal will cause scintillation, this is the pulse of light measured by the APD or vacuum phototriode. A typical pulse from an ECAL crystal is shown in the figure 4.5. This is a digitized pulse, and the solid lines represent simulated pulses for the in-time and out-of-time pile-up collisions. The simulated pulses are used to obtain a better estimate the effect of pile up in simulation.

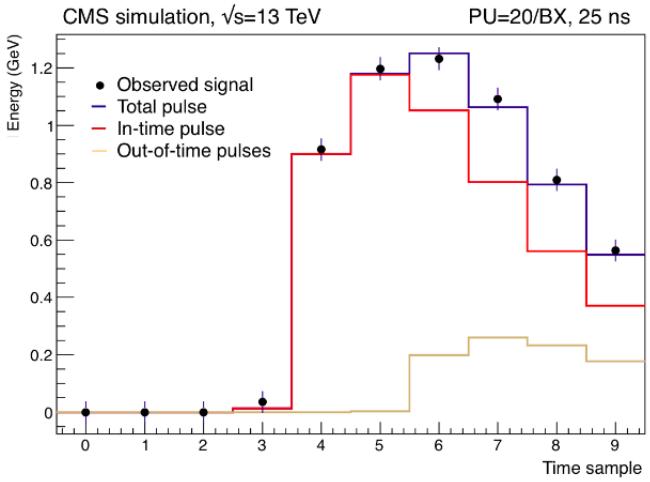

Figure 4.5: ECAL pulse and the templates used to minimize the χ^2 fit

The ECAL barrel is made of 61,200 crystals, with dimensions of 2.2cm×2.2cm×22cm, organized in 36 super modules. They have a radiation length of $X_0 = 89$cm and a Moliere radius of $R_0 = 2.19$cm. These paramaters ensure the containmnet of the electromagnetic shower within one crystal. The crystals are arranged using the $\eta \times \phi$ coordinate system as shown in the figure below.

The ECAL endcap is composed of 14,648 crystals, with dimensions 2.9cm×2.9cm×22cm, organized in 4 Dees. In front of the crystal layer lies the pre-shower, which is composed of layered lead and silicon strips. The pre-shower is added to provide an extra layer of tracking before photons reach the crystals. When the photons reach the lead layer, the interaction will induce the start of an electro-magnetic shower. The main purpose of the pre-shower is to add extra granularity to resolve π^0 events from single photon events in the high η region.

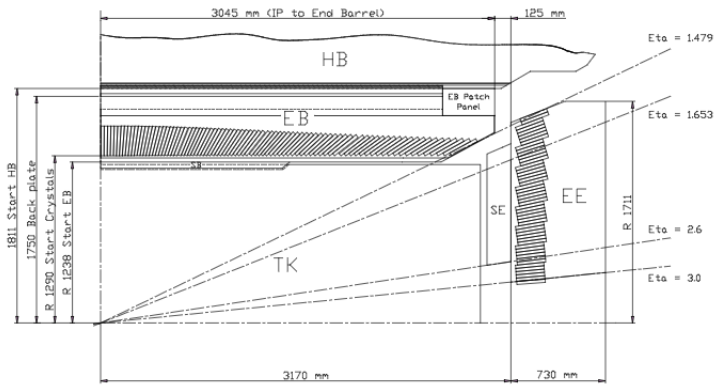

Figure 4.6: ECAL geometry.

4.4.1 Amplitude Reconstruction

The pulse amplitude from a single crystal is the most important quantity to experimentally measure. The energy of a photon or charged particle in the ECAL (determening the energy goes well beyond hardware level). The amplitude is determined by sampling the pulse in 10 different regions and then minimizing the following χ^2 equation.

$$\chi^2 = \sum_{i=1}^{N} \frac{(\sum_{j=1}^{M} A_j p_{ij} - S_i)^2}{\sigma_{S_i}^2}$$

where A_j is the amplitude from the jth interaction (simulation), p_{ij} is the function (template) evaluated at the ith sample for the corresponding pulse from the jth interaction, S_i is the ith sample from the pulse [10].

4.4.2 Clustering

Amplitude reconstruciton is at the lowest level of object identification, the next level involves the clustering of triggered crystals and the measurement of the energy of an

electron or photon. The following figures illustrate how clustering of an electron or photon is done. The island algorithm [9] works by taking a seed crystal (the crystal with the most energy deposited) and iteretevely scanning for continous energy reduction in η steps and ϕ rings. The algorithm stops when it finds a crystal that has not been triggered or is rising in energy. Once it stops in one η direction it moves in the opposite direction and the same iterative procedure is carreied out. This is to form a single cluster, typically the electron will bremstrahlung as it interacts with the material from the tracker. This radiation will mostly spread along the ϕ direction. Therefore, it is also necessary to create a cluster of clusters, superclusters, to capture all the energy of an electron. The superclustering algorithm takes into account neighboring clusters and uses geometric restrictions to determine the spatial boundaries of the supercluster. For Run II, a new method called the mustache algorithm takes into account the spread of the shower along both η and ϕ direction. The idea is to account for the bending along this direciton due to the magnetic field.

4.5 Hadronic Calorimeter

The Hadron Calorimeter is responsible for measuring the energy of hadronic jets. Hadronic jets are produced when a initial or final state gluon is radiated, or quark is knocked off (from a proton) or produced during a collision. While the ECAL will contain most of the photons and electrons, heavier objects like muons and hadronic jets, have enough energy to go through the ECAL and deposit most or some of their energy in the HCAL. The HCAL primaraly consists of alternating layers of brass plates and organic scintillators. The brass plates are used as stoppers to slow the particles so that the particle or jet can be contained

within the HCAL layer. Brass stoppers have to be used to meet the limitations imposed on by the compactness of CMS; from the center of the beam pipe to the outer radius of the solenoid, the radius is about 3.0 m and the tracker plus ECAL material takes up about 1.6 m without counting for extra material budget like cabling and empty spaces. These makes the effective length of the HCAL barrel to be 1 m. The HCAL barrel is also arranged in the $\eta \times \phi$ direction and it aligns along the same coordinate axis with muon chambers and the ECAL. The end cap of the HCAL is consisists of 36 megatiles arranged ϕ wedges. In the outer solenoid region, the outer HCAL is used to measure hadronic showers that don't impinge all their energy in the HCAL barrel or for showers that start later in the barrel material.

4.6 Solenoid

The solenoid of CMS provides an maximum operating magnetic field of 3.8 T. It has a free bore of 6.0 m and a lenght of 12.5 m. The magnet is encased (surrounded) by an iron yoke, this is to ensure magnetic field homogeneity.

4.7 Muon Systems

The muon system is composed of a mix of Resistive Plate Chambers (RPCs), Cathode Strip Chambers (CSCs), and Drift Tubes (DTs). The RPCs are composed of a gas sandwiched between to high resistivity ceramic plates, with readout strips on top of the resistive plate. The CSCs are also modules full of gas but with anode wires running

horizontal to the lenght of the module and cathode strips running vertically along the lenght of the module; with this two coordinates each module can pinpoint the impact point fo the ionizing particle. DTs are tubes filled with a gas and a single wire with two electrodes on either side (usually on the coordinate being measured).

4.8 Trigger

The CMS trigger system consists of several stages but only one online stage, this is the L1 trigger. The L1 trigger is a hardware based trigger that does low level reconstruction of physics objects. These include simple threshold triggers on the ECAL or HCAL for example. The L1 trigger takes information from each subdetector (except the silicon tracker) and combines this information in several stages to make a final decision. This decisison is then sent back to detectors so that they can read out by the central CMS DAQ.

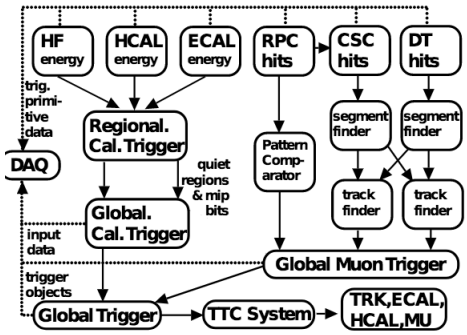

Figure 4.7: L1 trigger schematic, there are no silicon tracker primitive tirggers, work is ongoin to develop a track trigger for phase II of the LHC

Offline, once event data has triggered CMS, a High Level Trigger (HLT) runs complex physics algorithms to determine if the event is of any scientific interest.

Chapter 5

Two Photons in CMS

5.1 The Two Photon Signal

The gluon-gluon Parton Distribution Function (PDF) has the highest probability of collisions for the possible momentum exchanges at the energies of the LHC. Consequently, gluon-gluon fusion (GGF) is the most common higgs production channel. The GGF cross section has a theoretical value of σ_{ggh}= 48.58 pb [7]. The next production process that dominates at the LHC is *Vector Boson Fusion* (VBF) with a theoretical cross section of σ_{vbf}= 3.87 pb. The *higgssstrahlung* (VH) and *top-top annahilation* (TTH) are in similar order to VBF. With a rounded measured luminosity of $\mathcal{L}$= 40.0×10^3 pb^{-1} it is clear that GGF will be the most abundant process at the LHC. An estimated yield of $N_{ggh} \sim 2\times10^6$ events with VBF $N_{vbf} \sim 1.5\times10^5$ given $N_x = \mathcal{L} \times \sigma_x$. With the fraction of these events going to two photons at roughly 0.1% the expected number of events is dramatically reduced to $N_{ggh} \sim 2.0\times10^3$. These numbers are also subject to the selection *efficiency* and the detector

acceptance. The most dominant background has a cross-section of over 2000 times greater than the GGF process.

From plots in figure 5.1 it is clear that the two photon channel has the lowest branching ratio of all the other possible decays at the LHC. Despite this-and the messy collison environment-the two photon channel (and the four lepton channel) is the cleanest higgs decay that can be measured at the LHC.

5.2 Two Photon Background

Backgrounds for the two photon analysis are non-signal events that also decay into two photons within the signal region, these can either be fake photons (other decay objects mimicking a photon within CMS) or real photons (prompt). The main sources for *prompt-prompt* background are born scattering of quarks, and *gluon-gluon* scattering through a qaurk loop. Electrons and jets in the event are the main sources of fake photons. An electron without a track assigned to it is just a hit in the ECAL, a jet wich deposits sufficient energy within the ECAL can also fake a photon, any ocurrence of the two of these type of effects can be interpreted as a fake two photon event. It is a very complex task to model these effects in simulation and theory. The analytical structure of the two photon invariant mass ($m_{\gamma\gamma}$) spectrum is therfore not known *a priori*. Fortunately, the spectrum is smooth and falling with $m_{\gamma\gamma}$ while the higgs signal is a sharp distribution centered around $m_{\gamma\gamma} = 125$ GeV. This contrast in shape make it simple to do a bump finding search.

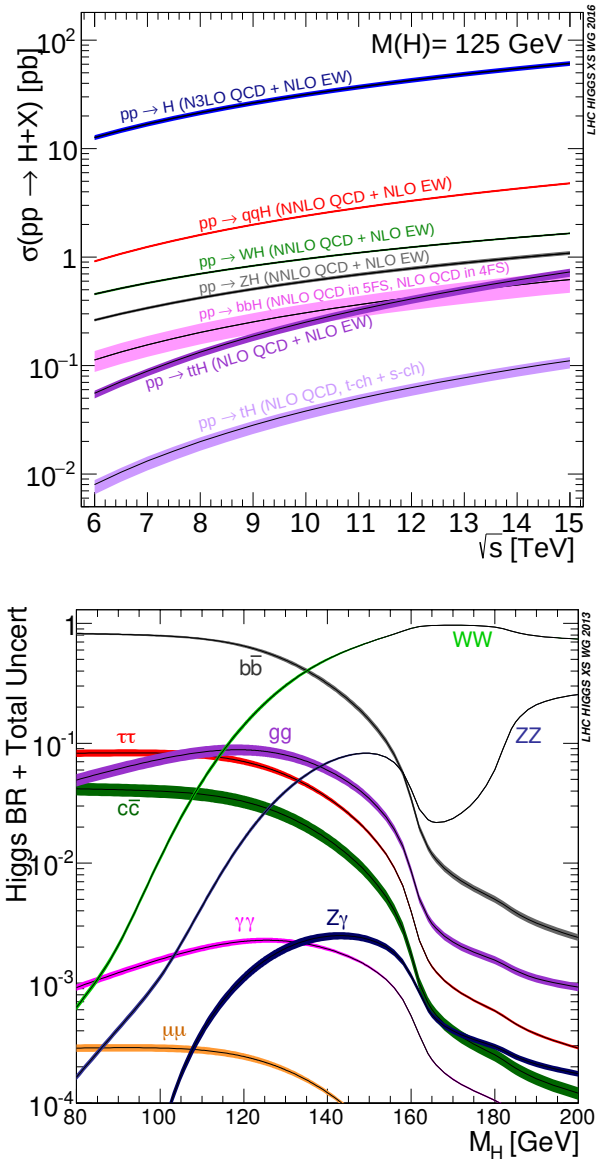

Figure 5.1: Higgs production cross-sections as a funciton of collision energy and higgs decay branching ratios as a function of collision energy

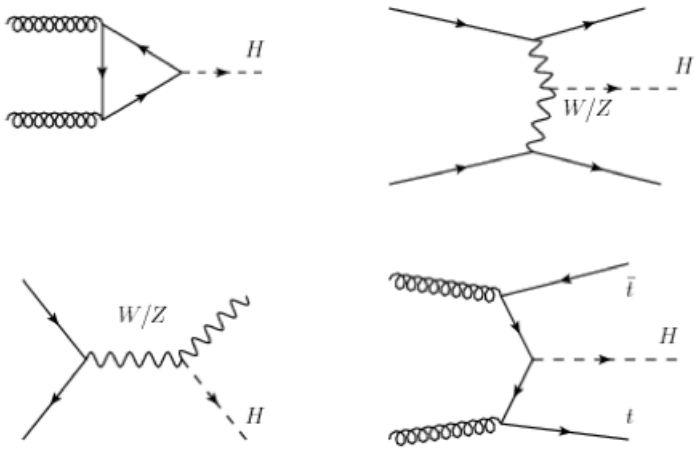

Figure 5.2: Feynman diagrams for each of the major production channels.

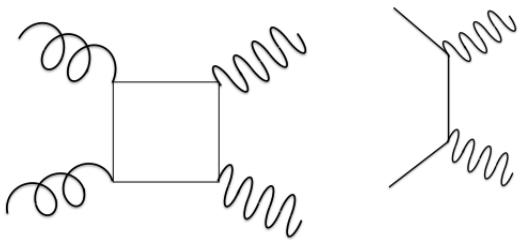

Figure 5.3: Feynman digrams representing the major QCD contribution to the irreducible diphoton background.

Chapter 6

$H \rightarrow \gamma\gamma$ Object Selection

6.1 Analysis Overview

The $H \rightarrow \gamma\gamma$ analysis is split into two main parts. The first part defines and applies cuts and or algorithms on physical variables of interest, it also provides the first level of event interpretation. The second part deals with the statistical analysis from the output of the physics selection. This is where the signal model and background model are built and results are produced. After 2013, when the full analysis of the combined 7TeV and 8TeV data samples was finished, an effort started to centralize the software framework to make it more accessible and easier to manage. With data accumulating faster during Run II, it was also important to control the size of the samples. Both of these factors were taken into account in the new analysis software framework, Fast Lightweight Analysis Steps for Higgs to gamma gamma (FLASHgg).

6.2 Monte Carlo Samples

Simulated samples play a major role in this analysis. Good simulations of the background and signal help to improve the training of a BDT. It also allows for less uncertainty in data/MC differences and a better understanding of the detector systematics. Each higgs production process has a dedicated MC sample at different mass points. The GGF,VBF,TTH and VH samples use 120, 123, 124, 125, 126, and 127 GeV higgs mass points. The main background samples are the *GammaJet* sample, this is a good source of *prompt-fake* photons (a misreconstructed jet can fake a photon). The *DiphotonBox* sample involves diphoton production through a quark box diagram and is a good sources of irreducible background. The QCD samples simulate another source irreducible background and account for the Born process for strong diphoton production, and finally the Drell-Yan sample simulates *fake-fake* photons where the fake photons are misrecunstructed leptons. The main generator used for the signal MC generation is Pythia8.

Bkg. samples	GJet_Pt-20to40_DoubleEMEnriched_MGG-80toInf_TuneCU_8M1_13TeV_Pythia8
	GJet_Pt-40toInf_DoubleEMEnriched_MGG-80toInf_TuneCU_8M1_13TeV_Pythia8
	QCD_Pt-30to40_DoubleEMEnriched_MGG-80toInf_TuneCU_8M1_13TeV_Pythia8
	QCD_Pt-40toInf_DoubleEMEnriched_MGG-80toInf_TuneCU_8M1_13TeV_Pythia8
	DiPhotonJetsBox_MGG-80toInf 13TeV-Sherpa
	DYJetsToLL_M-50_TuneCU_8M1_13TeV-amcatnloFXFX-pythia8

Table 6.1: Background MC samples.

Main signal samples	GluGluHToGG_M125_13TeV_amcatnloFXFX_pythia8 VBFHToGG_M125_13TeV_amcatnlo_pythia8 VHToGG_M125_13TeV_amcatnloFXFX_madspin_pythia8 ttHJetToGG_M125_13TeV_amcatnloFXFX_madspin_pythia8_v2

Table 6.2: Signal MC samples.

6.3 Data Samples

Each data sample corresponds to different periods of LHC running. The total integrated luminosity of the samples below is 35.9 $fb^{-}1$. Other data samples were also used in the analysis, but these are not used to lookg for diphoton events.

6.4 Vertex Reconstruction

The position of the collision vertex is one of the most important measurements in this analysis. To determine the correct collision vertex a BDT is used and is trained with signal and backfround MC.

samples	/DoubleEG/Run2016B-03Feb2017 ver2-v2/MINIAOD /DoubleEG/Run2016C-03Feb2017-v1/MINIAOD /DoubleEG/Run2016D-03Feb2017-v1/MINIAOD /DoubleEG/Run2016E-03Feb2017-v1/MINIAOD /DoubleEG/Run2016F-03Feb2017-v1/MINIAOD /DoubleEG/Run2016G-03Feb2017-v1/MINIAOD /DoubleEG/Run2016H-03Feb2017 ver2-v1/MINIAOD /DoubleEG/Run2016H-03Feb2017 ver3-v1/MINIAOD

Table 6.3: 2016 Run2 data samples.

$$sumpt2 = \sum_i |\vec{p}_T^{\,i}|^2$$

$$ptbal = -\sum_i (\vec{p}_T^{\,i} \cdot \frac{\vec{p}_T^{\,\gamma\gamma}}{|\vec{p}_T^{\,\gamma\gamma}|})$$

$$ptasym = \frac{|\sum_i \vec{p}_T^{\,i}| - |\vec{p}_T^{\,\gamma\gamma}|}{|\sum_i \vec{p}_T^{\,i}| + |\vec{p}_T^{\,\gamma\gamma}|}$$

where *sumpt2* is the sum of the magnitudes of the transverse momentum of each track in the event. The vertex that maximizes this value is picked as the primary collision vertex by CMS. The *ptbal* variable takes the sum of the magnitude of the projected component along the diphoton direction of all the tracks. A high positive value of this variable would mean that the majority of the tracks have a high component along the diphoton direction, meaning that the reference vertex chosen to reconstruct the tracks does not reflect the recoil the system would experience from a hard collision. On the other hand, a negative value would mean the opposite, thus reflecting the recoil of the system from the hard collision. The *ptasym* variable quantifies the assymetry of the system (all the tracks in the event), a wrong vertex would make the vetor sump of all the tracks pt equal to zer0, making the value of *ptasym* equal to negative one. We know that transverse momentum should be conserved, this would imply that the system shuold be closely balanced with the diphoton, therefore it is expected that the difference should be small and with a value of *ptasym* less than one.

6.5 Vertex Probability

Once the vertex has been classified and the vertex with the highest MVA score has been selected, it is essential to know the probability that the correct vertex has been

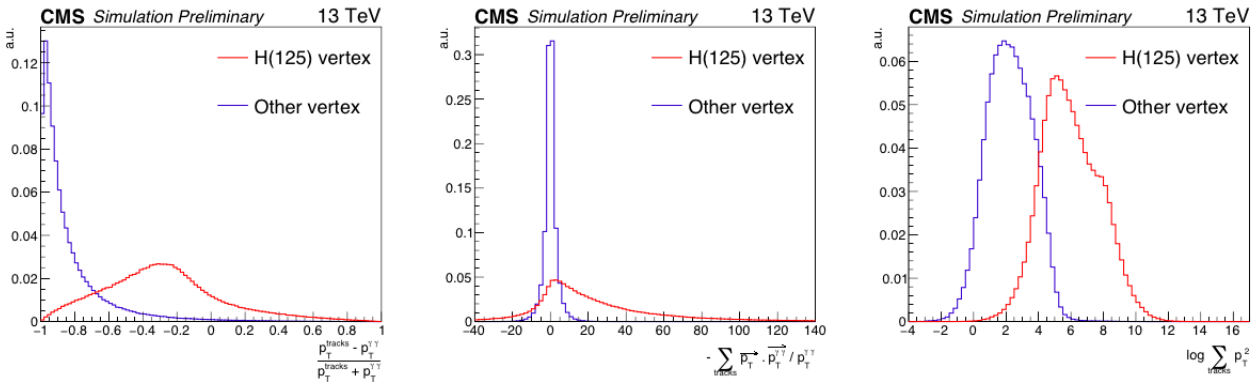

Figure 6.1: Vertex ID varibale shapes for the signal vertex and the background vertex

chosen. To give such a value per vertex id score a new BDT is trained. The variables are:

- The diphoton p_T,
- The number of vertices in the event,
- The vertex id score for the best three vertices,
- The longitudinal distance between the chosen vertex and second and third best vertices,
- The number of converted photons

The fraction of vertices within 1 cm of the true vertex (generator level vertex) per event is assaigned to the output of the vertex probability MVA output. A 4^{th} order function is then fitted to the shape of this distribution, and the probability value for each event is extracted based on its vertex probability score.

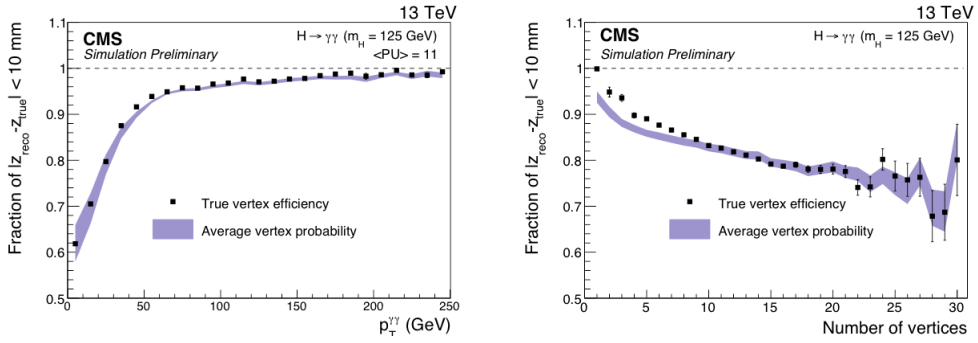

Figure 6.2: Vertex ID and vertex probability plots

6.6 Vertex ID Validation

In order to guarantee that the vertex algorithms will work in data the variables and performance are validated using Z→ $\mu\mu$ events. The dimuon event vertices are first refitted without the muon tracks to emulate photons, the new selected vertex is then compared to the original vertex with the muon tracks.

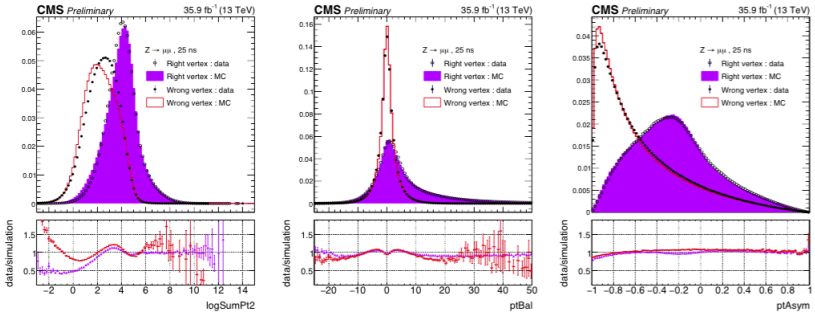

Figure 6.3: Vertex id variables validation

6.7 Photon Energy Reconstruction

The energy of each photon that goes into the analysis is further corrected to account for more subtle detector effects in the ECAL and for run dependent conditions. Effects such a shower containment in the ECAL, loss of energy due to the cracks between crystals and crystal trasnperancy affects have to be taken into account for a good measurement of the energy.

6.7.1 Photon Energy Regression

For Run2, the shape of a single photon's E_{gen}/E_{RAW} distribution is assumed to be a double crystal ball. Each parameter of the crystal ball function is then determined by boosted regression (the phase space of input variables maps unto unique double crystal ball functions). This gives a per photon mass resolution estimate which can then be used to calculate per event diphoton mass resolution estimate. This estimate is later used to classify signal diphotons.

6.7.2 Photon Energy Smearing Corrections

Even with these corrections, there are still left over differences between data and MC. These differences tend to be more dependent on run time conditions and are hard to model or predict in same way as global containment corrections. The Z mass scale in data is correceted so that it matches the scale in MC. Once the scale has been matched for both data and MC, the MC is smeared to match the data.

6.8 Photon Selection And Reconstruction

Photons go through two levels of reconstruction, with the second level tailored to this analysis. In the fisrt level of reconstruction photons are identified by the differences in the electromagnetic (EM) shower shape. The main tool used for reconstruction and identification is the Particle Flow algorithm (PF). The PF algorithm is responsible for the reconstruction of particles using information from all detectors. Most of the photon energy can be accounted for in the mustache algorithm metioned earlier in chapter 3. Using reconstructed PF photons from a prompt photon rich sample, a BDT is trained to tell photons apart from two merged superclusters coming from the decay of a neutral meson into a pair of boosted photons. The variables used in the BDT are:

- $E_{2\times2}/E_{5\times5}$: The energy of a 2×2 cluster containing the first and second most energetic crystals divided by the energy in a 5×5 cluster centered around the supercluster seed.
- $cov_{i\eta\phi}$: The covariance of the electromagnetic shower spread in η and ϕ directions within the $E_{5\times5}$ supercluster in a crystal by crystal basis.
- $\sigma_{i\eta i\eta}$: The variance in the η direction within the $E_{5\times5}$ supercluster in a crystal by crystal basis.
- R_9: $E_{3\times3}/E_{SC}$ where $E_{3\times3}$ is a 3×3 cluster around the seed crystal and E_iSC is the energy from the particle flow energy sharing algorithm.
- σ_η: Logarithmic energy weighted varince of single crystal η within the supercluster.
- σ_ϕ: Logarithmic energy weighted varince of single crystal ϕ within the supercluster.

- PF Photon Isolation: The transverse energy sum within a cone of ΔR=0.3 associated with energy produced by photons with ρ correction applied.
- PF Charged Isolation w.r.t. wrong vertex: The energy associated with charged particle candidates within a cone of ΔR=0.3 around the photon candidate and with respect to the wrong vertex.
- PF Charged Isolation w.r.t. correct vertex: The energy associated with charged particle candidates within a cone of ΔR=0.3 around the photon candidate and with respect to the right vertex.
- ρ: The transverse energy contribution from pile up around a cone of ΔR=0.3.
- Supercluster η: The supercluster pseudo-rapidity.
- E_{RAW}: The supercluster energy.

In the endcap region the the following variables are added to the training:

- E_{PS}/E_{RAW}: The pre-shower measured energy divided by the supercluster energy.
- σ_{RR}: The variance in the electromagnetic shower spatial spread in the radial direciton of the pre-shower.

The BDT will learn how background events look vs signal events, specifically it will learn the shower shape of neutral meson events vs *prompt* photons. This is clearly reflected on the variable selection, the spatial shape of the shower plays a big role in the training. The isolation variables account for the expected background contributions to the

isolation, a highly isolated photon will not have many charged candidate contributions on the cone, while a fake photon from a neutral meson decay will do due to hadronic activity. To garantee that the BDT will work for selecting photons a dedicated validation of the algorithm is done with Z→ee events, where the tracks from the electrons are removed. To ensure electrons are originating from a Z boson the invariant mass of the dielectron system needs to be between 70 GeV and 110 GeV. Additional cuts are applied on the leading and subleading transverse momentum, these are 40 GeV and 30 GeV respectevely. The trigger used for data is HLT_Ele27_WPTight_Gsf.

6.9 Trigger

A diphoton HLT trigger is used for this analysis. The diphoton HLT is seeded by at least one L1 photon candidate. During Run1 the lowest transverse momentum a L1 photon seed could have was 25 GeV, for Run2, the event rate had to be mitigated and the single photon L1 seed had to be increased to 40 GeV. This significantly reduced the HLT efficiency and a new strategy was implemented. To the same path an L1 diphoton pair was added, so instead of seeding the HLT only with single photon L1 seeds, lower transverse momentum pairs can also seed the HLT. Using this strategy, subleading photons can have a transverse momentum of 15 GeV, with these low energy photons being recuparated the efficiency of the HLT was restored. The HLT path used in the analysis HLT_Diphoton30_18_R9Id_OR_IsoCaloId-160_AND_HE_R9Id_Mass90.

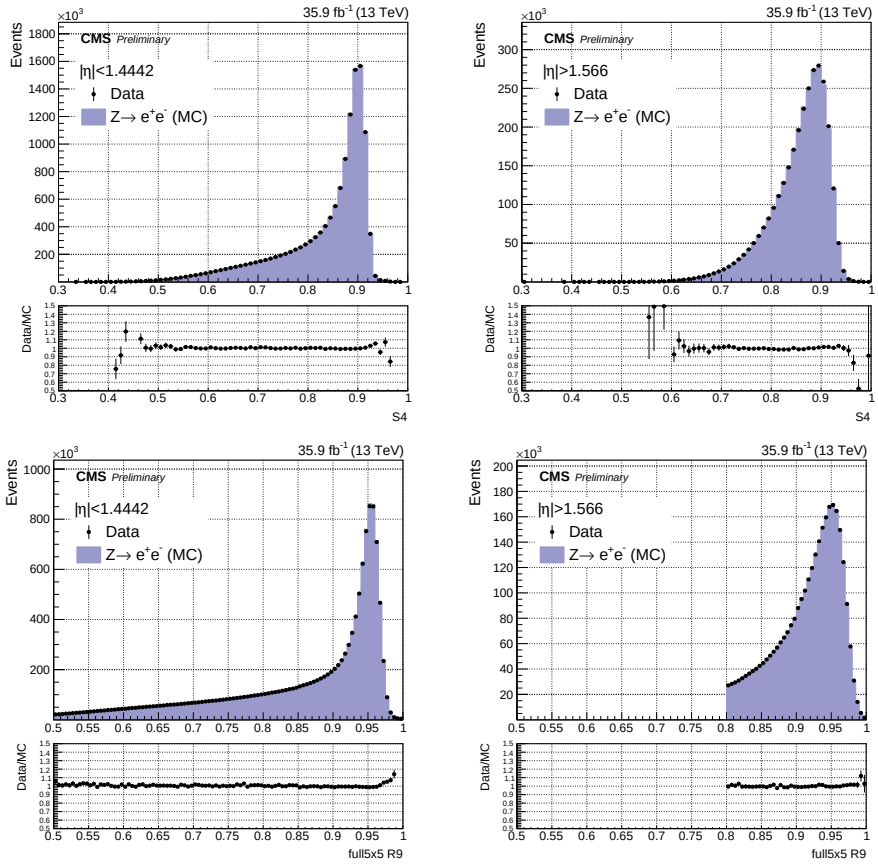

Figure 6.4: Cluster variables, the left plots are for EB and the right plots are EE

6.10 Pre-selection

Since the HLT is not applied to MC, a pre-selection is applied in order to have a common initial phase space both in data and MC. The pre selection is tighter than the trigger. All samples go trough the pre-selection before entering the full analysis. The pre-selection is also validated using using Z→ee data samples, and the efficiency is measured usinf the tag and probe technique.

	H/E	$\sigma_{i\eta i\eta}$ 5×5	R9(5×5)	pfPhoIso	TrackerIso
$\|\eta\| < 2.5$, R9 < 0.85	<0.08	-	>0.5	-	-
$\|\eta\| < 2.5$, R9 ≥ 0.85	<0.08	<0.015	> 0.5	< 4.0	< 6.0
$\|\eta\| > 2.5$, R9 < 0.85	<0.08	-	> 0.8	-	$<$ -
$\|\eta\| > 2.5$, R9 < 0.85	<0.08	<0.035	> 0.8	< 4.0	< 6.0

6.11 Diphoton Classification

With individual photon objects fully reconstructed and the event vertex selection fully optimized, diphoton objects can now analyzed. For events that cannot be fully interpreted, meaning that the production process cannot be determined, it is essential to have a handle on how signal like a diphoton is. This achieved with a boosted decision tree, that is trained against signal and background. The point of using a classifier is to be able to categorize diphotons based on their resolution, purity, and good signal kinematics. It is also possible to fully interpret the event by its produciton mechanism using other reconstructed objects. The majority of events though will come from GGF production which cannot be fully reconstructed since there are no good secondary objects that can be analyzed (therefore it is assumed that events that are not interpreted as VH,VBF or TTH will come from GGH). The variables used to achieve this are:

- Both photons' $pt_T/m_{\gamma\gamma}$,
- Both photons' η,
- The cosine of the angle between the photons in the transverse plane, $\cos(\Delta\phi)$,
- The photon id value for both photons,
- The per-event mass resolution of the diphoton under the assumption that the correct

vertex was chosen $_{rv}$.

- The per-event mass resolution of the diphoton under the assumption that the wrong vertex was chosen σ_{wv}.

- The per-event vertex probability of the chosen vertex *pvtx*

σ_{rv} and σ_{wv} are calculated using the per-photon energy resolution,

$$\sigma_{rv} = \frac{\sigma_m^{right}}{m_{\gamma\gamma}} = \frac{1}{2}\sqrt{(\frac{\sigma_{E_1}}{E_1})^2 + (\frac{\sigma_{E_2}}{E_2})^2}$$

$$\sigma_{wv} = \frac{\sigma_m^{wrong}}{m_{\gamma\gamma}} = \sqrt{(\frac{\sigma_m^{right}}{m_{\gamma\gamma}})^2 + (\frac{\sigma_m^{vtx}}{m_{\gamma\gamma}})^2}$$

where σ_m^{vtx} is the distance between the correct vertex and the selected primary vertex. The BDT is provided extra information on the signal to background relation with the diphoton resolution. This is done by weighting the signal events by $w_{sig} = \frac{p_{vtx}}{\sigma_{rv}} + \frac{1 - p_{vtx}}{\sigma_{wv}}$. In this way events with a high resolution and high probability of choosing the correct vertex will have a much higher weight than those with a bad resolution and low probability of choosing the correct vertex. This will corrolate high resolution to signal purity. The plots in figure blah show the input variable distributions.

The diphoton MVA has to also be validated, this is done using Z→ee data events. The electrons are stripped from their tracks and reconstructed as photons. These emulated photons then are subject to the same selection as regular photon objects. The weights from the diphoton MVA original traning are then used to classify the emulated photons. Data-MC comparisons are made using Z→ee data and MC.

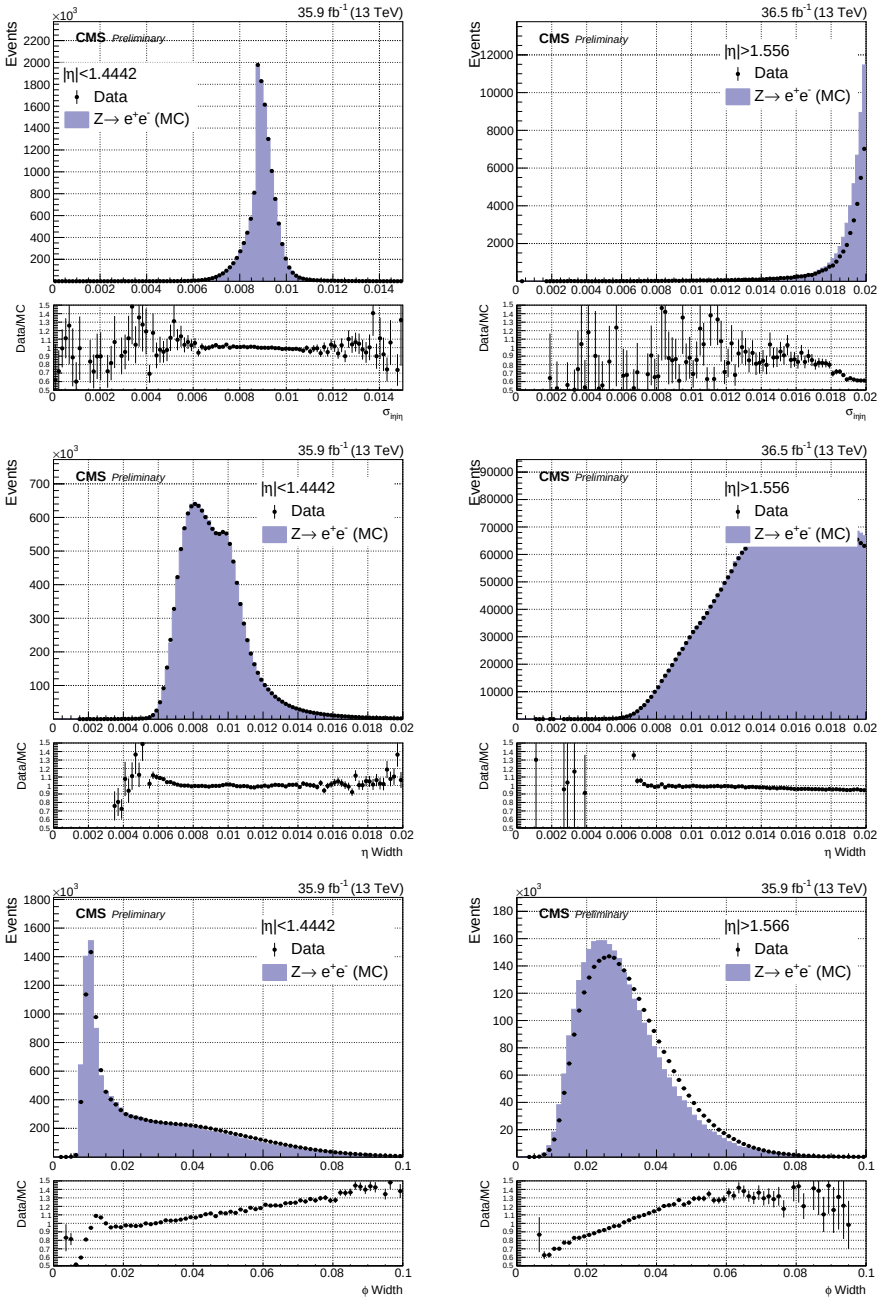

Figure 6.5: shower shape variables, the left plots are for EB and the right plots are EE

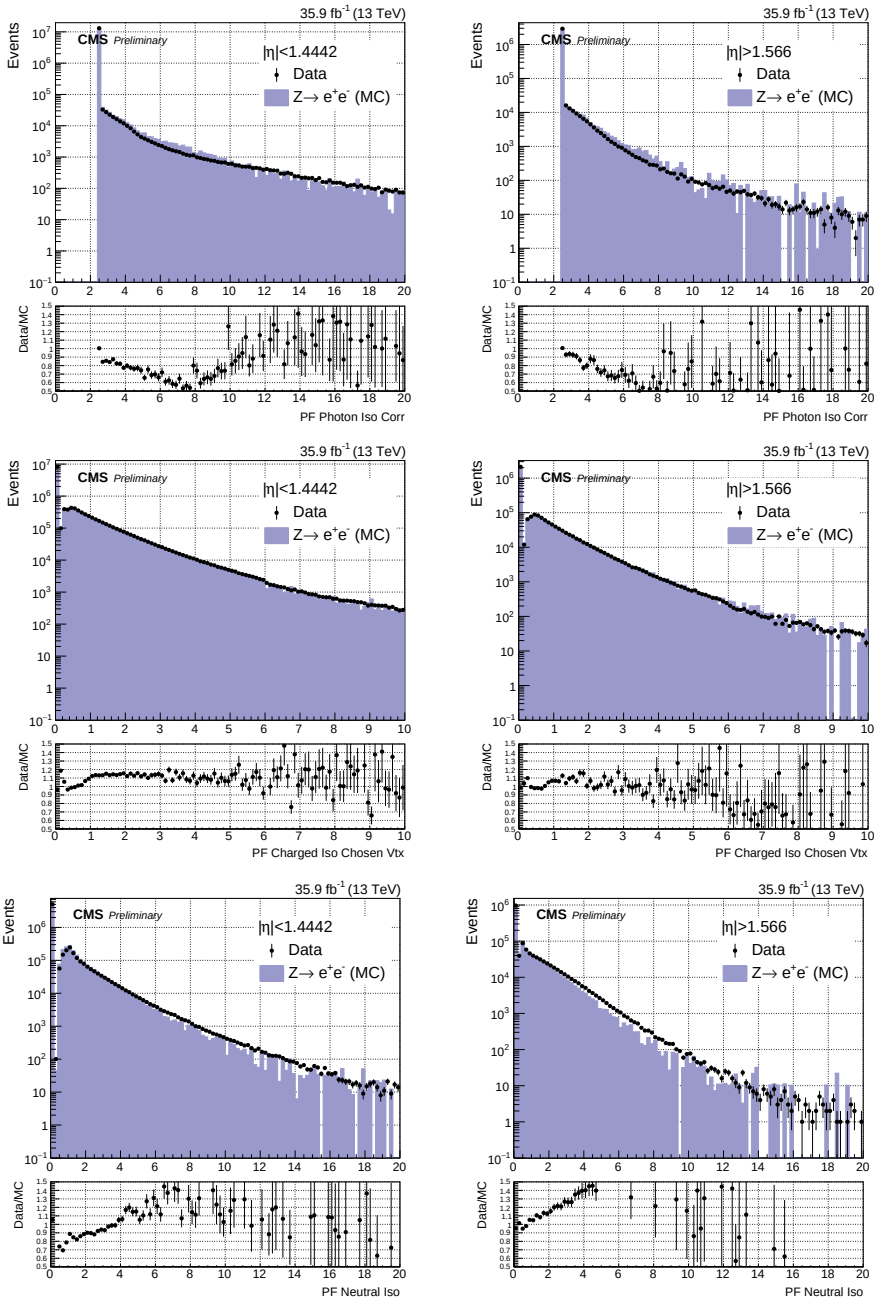

Figure 6.6: Isolation variables, the left plots are for EB and the right plots are EE

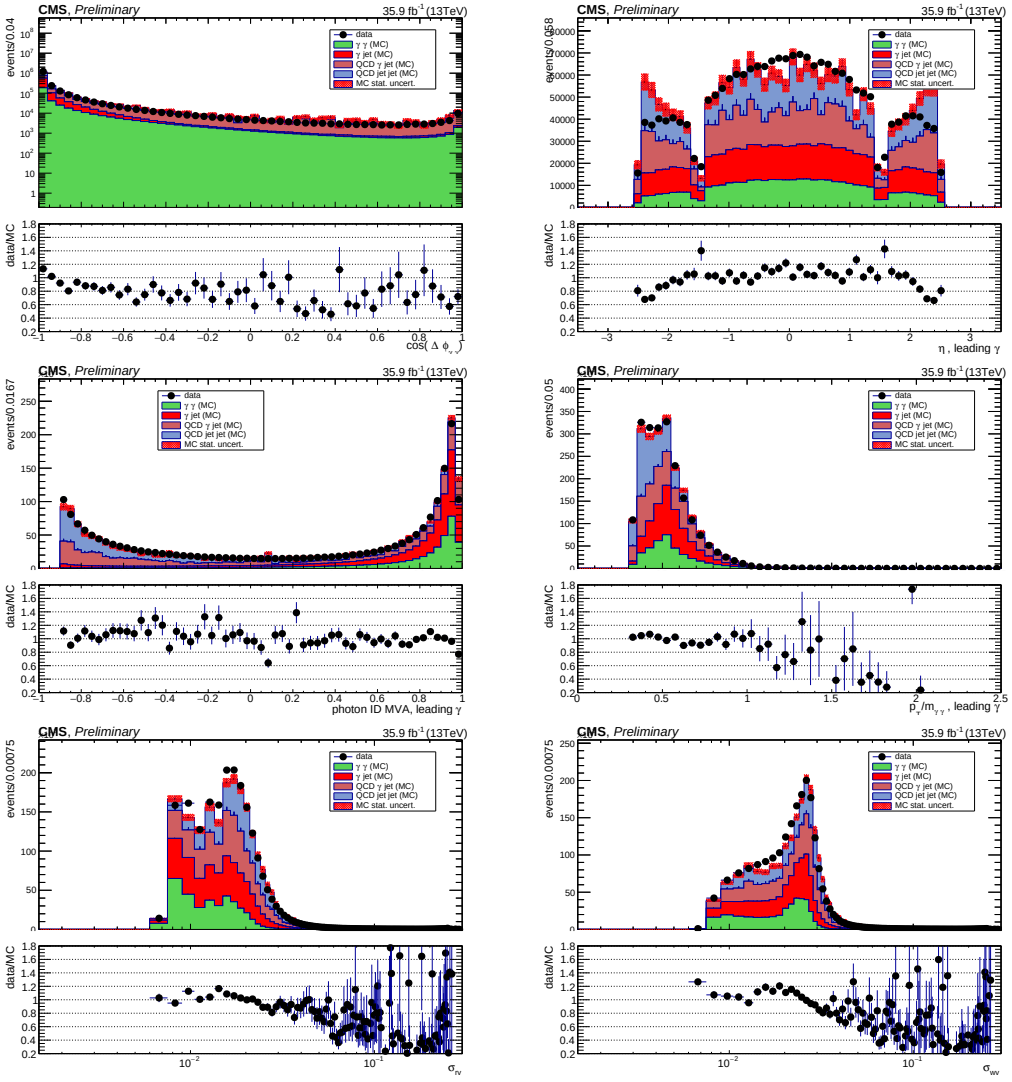

Figure 6.7: Data-MC comparisons for the diphoton MVA input variables, the histograms are normalized to the area and wighted by their cross-section.

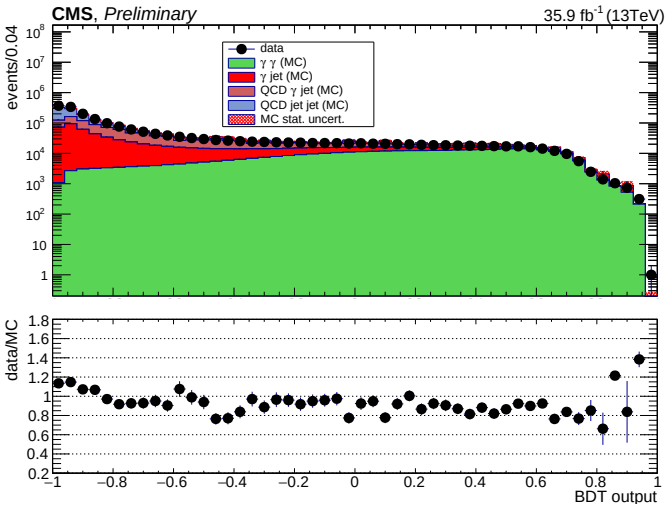

Figure 6.8: Data-MC comparisons for the diphoton MVA result, the histograms are normalized to the area and are weighted by their cross-section.

Chapter 7

H→$\gamma\gamma$ Event Selection

The events are divided into different categories to maximize the signal to background ratio. An event can meet the requirements of multiple categories, but priority is given to the category with the highest purity. The purest categories will therefore be leptonic. Categories in which no higgs production process can be determined are label as Untagged categories, the rest of the events then fall unto subcategories of the TTH,VH or VBF processes, the catefories are:

- TTH Categories:
  - TTHLeptonicTag: top-antitop production of the higgs with leptonic decays.
  - TTHHadronicTag: top-antitop production of the higgs with hadronic decays.
  - TTHHadronicMVATag: New Run2 method using an MVA to categorize hadronic decays in top-antitop higgs production.
- VH Categories:

  - ZHLeptonicTag: The purest category in the analysis, the aim of this category is to collect *higgstrahlung* events with a leptonically decaying Z boson.
  - WHLeptonicTag: *Higgstrahlung* production of the higgs with a W boson decaying leptonically.
  - VHLeptonicLooseTag: *Higgstrahlung* production of the higgs with a W boson with decaying leptonically but with lower missing energy than WHLeptonic.
  - VHHadronicTag: *Higgstrahlung* production of the higgs boson with a W or Z boson decaying hadronically.
  - VHMetTag: *Higgstrahlung* production of the higgs boson with a Z boson decaying into a pair of neutrinos or a W boson decaying leptonically with a misreconstructed lepton.

- VBF Categories:
  - VBFTag0,1,2: Vector boson fusion production of the higgs, an MVA method is used to categorize such events by taking advantage of the dijet system kinematics.

- Untagged Categories:
  - UntaggedTag0,1,2,3: Unclassified diphoton events which are categorized based on their diphoton mva score, lowest category corresponding to low resolution and low signal to background ratio.

7.1 TTH Categories

7.1.1 TTHLeptonicTag

This category looks for leptonically decaying tops from the top-antitop production process, i.e. $t\bar{t} \rightarrow bl\nu_l\bar{b}l\nu_l$,$bl\nu_l\bar{b}q\bar{q}$. It asks for at least on good lepton and has additional requirements for jets. The set of cuts are:

- electron or muon p_T >20 GeV
- muon $|\eta|$ <2.4
- $p_T^{lead}/m_{\gamma\gamma}$ >0.5
- $p_T^{sublead}/m_{\gamma\gamma}$ >0.25
- Diphoton MVA score >-0.405
- Photon MVA score >-0.9
- $\Delta R_{\mu\gamma}$ >0.35
- $\Delta R_{\mu jet}$ >0.4
- ΔR_{ejet} >0.4
- N_{jets} >2
- N_{bjets} >1
- p_T^{jet} >25 GeV

- Jet $|\eta|$ <2.4
- $\Delta R_{jet\gamma_{lead}}$ >0.4
- $\Delta R_{jet\gamma_{sublead}}$ >0.4
- μPFIsoSumRelThreshild >0.25
- μPFIsoSumRelThreshold >0.6
- PuIDCutoffThreshold >0.8
- ΔR between the electron track and the supercluster coordinates <0.25
- $d_{xy}EB$ >0.0261
- d_zEB >0.41
- $d_{xy}EE$ >0.118
- d_zEE >0.822
- $\Delta R_{\gamma e}$ 0.35
- $|m_{e\gamma} - m_Z|$ <5.0 GeV
- electron:
  - full5x5_$\sigma_{i\eta i\eta}$ <0.0314
  - $\Delta\eta_{inSeed}$ <0.00868
  - $|\Delta\phi_in|$ <0.213

- H/E <0.101
- PFIso with effective area corr <0.107
- $|(1/E - 1/p)|$ <0.14
- expected missing inner hits $\leq$1
- pass conversion veto = yes

– $|\eta|$ <2.5 or, 1.4442 <η<1.556

7.1.2 TTHHadronicTag

The TTHHadronic Tag looks for hadronic final states from top-antitop production. The event reconstruction requires at least 1 b-jet and looks for a total at leat 5-jets. The selection is as follows:

- p_T^{lead} >0.5
- $p_T^{sublead}$ >0.25
- Diphoton MVA score >-0.405
- Photon MVA score >-0.9
- jet_{p_T} >25.0 GeV
- Jet $|eta|$ >2.4
- N_{jets} >5
- N_{bjets} >1

- $\Delta R_{jet\gamma_{lead}}$ >0.4
- $\Delta R_{jet\gamma_{sublead}}$ >0.4

7.2 VH Categories

The VH category is designed to take advantage of signal topologies that reflect W and Z boson decays after they radiate a higgs particle. All categories, except VHLeptonicLooseTag, have well defined topologies (WHLeptonic and ZHLeptonic are designed to classify leptonic decays of W and Z bosons, VHHadornic is designed to classify events with hadronically decaying W and Z bosons, and VHMet is designed to classify Z boson decay into neutrinos or large missing energy events that may have an unreconstructed photon), VHLeptonicLooseTag is designed to capture events with a good lepton but with less missing energy than WHLeptonicTag. The events which are fully categorized under the VH process are later used to measure the coupling of vector bosons to the higgs boson.

7.2.1 ZHLeptonicTag

Here a Z boson is reconstructed by identifying two good leptons of opposite charge, same flavor, and an invariant mass within tolerance of m_Z. The category defenition is:

- lepton p_T >20.0 GeV
- muon $|\eta|$ <2.4
- p_T^{lead} >.375
- $p_T^{sublead}$ >0.25

- Diphoton MVA score >-0.405
- Photon MVA score >-0.9
- $\Delta R_{\mu\gamma}$ >1.0
- $\Delta R_{e\gamma}$ >1.0
- $\Delta R_{\mu jet}$ >0.4
- 70.0 GeV <m_{ll} <110.0 GeV
- $d_{xy}EB$ >0.0261
- $d_z EB$ >0.41
- $d_{xy}EE$ >0.118
- $d_z EE$ >0.822
- $\Delta R_{\gamma e}$ 0.35
- $|m_{e\gamma} - m_Z|$ >0.5
- electron $|\eta|$ <2.5
- electron 1.566 <η<1.4442$ElectronIso$>0.15

- Muon Iso >0.25
- electron:
  - full5x5_$\sigma_{i\eta i\eta}$ <0.0314

- $\Delta\eta_{inSeed}$ <0.00868
- $|\Delta\phi_{in}|$ <0.213
- H/E <0.101
- PFIso with effective area corr <0.107
- $|(1/E - 1/p)|$ <0.14
- expected missing inner hits ≤1
- pass conversion veto = yes

7.2.2 WHLeptonicTag

WHLeptonic events will require one good lepton associated with high MET.

- MET >45.0 GeV
- electron or muon p_T >20 GeV
- muon $|\eta|$ <2.4
- p_T^{lead} >0.5
- $p_T^{sublead}$ >0.25
- Diphoton MVA score >0.0
- Photon MVA score >-0.9
- $\Delta R_{\mu\gamma}$ >0.35
- $\Delta R_{\mu jet}$ >0.4

- ΔR_{ejet} >0.4
- N_{jets} >3
- p_T^{jet} >20.0 GeV
- Jet $|\eta|$ <2.4
- $\Delta R_{jet\gamma_{lead}}$ >0.4
- $\Delta R_{jet\gamma_{sublead}}$ >0.4
- μPFIsoSumRelThreshild >0.25
- PuIDCutoffThreshold >0.8
- ΔR between the electron track and the supercluster coordinates <0.25
- $d_{xy}EB$ >0.0261
- d_zEB >0.41
- $d_{xy}EE$ >0.118
- d_zEE >0.822
- $\Delta R_{\gamma e}$ 0.35
- $|m_{e\gamma} - m_Z|$ >0.5
- electron:
  - full5x5_$\sigma_{i\eta i\eta}$ <0.0314

- $\Delta\eta_{inSeed}$ <0.00868
- $|\Delta\phi_in|$ <0.213
- H/E <0.101
- PFIso with effective area corr <0.107
- $|(1/E - 1/p)|$ <0.14
- expected missing inner hits ≤1
- pass conversion veto = yes

– $|\eta|$ <2.5 or, 1.4442 <η<1.556

The diphoton MVA cut was optimized by looking at the signal and background efficiency over different diphoton MVA values. At the discriminator value of 0.0, the tag retains 80 percent of the signal envents and rejects 50 percent of the background.

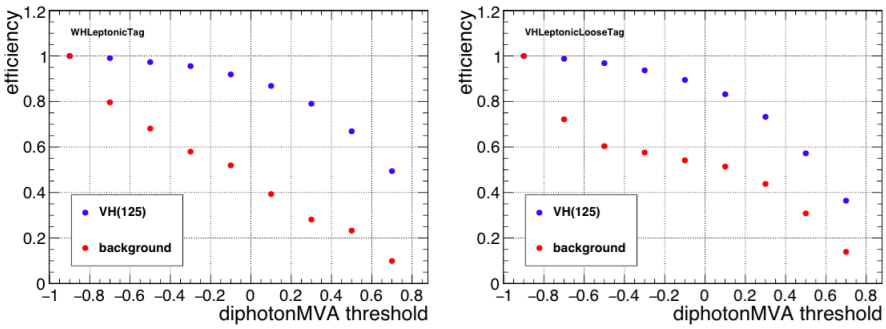

Figure 7.1: Tag efficiency as a function of diphoton MVA cut

7.2.3 VHLeptonicLooseTag

- MET <45.0 GeV

- electron or muon p_T >20 GeV
- muon $|\eta|$ <2.4
- p_T^{lead} >0.5
- $p_T^{sublead}$ >0.25
- Diphoton MVA score >0.0
- Photon MVA score >-0.9
- $\Delta R_{\mu\gamma}$ >0.35
- $\Delta R_{\mu jet}$ >0.4
- ΔR_{ejet} >0.4
- N_{jets} >3
- p_T^{jet} >20.0 GeV
- Jet $|\eta|$ <2.4
- $\Delta R_{jet\gamma_{lead}}$ >0.4
- $\Delta R_{jet\gamma_{sublead}}$ >0.4
- μPFIsoSumRelThreshild >0.25
- PuIDCutoffThreshold >0.8
- ΔR between the electron track and the supercluster coordinates <0.25

- $d_{xy}EB$ >0.0261
- d_zEB >0.41
- $d_{xy}EE$ >0.118
- d_zEE >0.822
- $\Delta R_{\gamma e}$ >0.35
- $|m_{e\gamma} - m_Z|$ >5.0 GeV
  - full5x5_$\sigma_{i\eta i\eta}$ <0.0314
  - $\Delta\eta_{inSeed}$ <0.00868
  - $|\Delta\phi_in|$ <0.213
  - H/E <0.101
  - PFIso with effective area corr <0.107
  - $|(1/E - 1/p)|$ <0.14
  - expected missing inner hits ≤1
  - pass conversion veto = yes
- $|\eta|$ <2.5 or, 1.4442 <η<1.556

The diphoton cut that is common to both WHLeptonicTag and VHLeptoniLooseTag was tried to be optimized by a different method. The strategy for optimization involves three steps. The first step is to obtain a control sample that can be used as a good estimation of the background distribution for these tags, since these categories do not have high statistics

it is important to not further restrict the category. The definition for the control sample used for this study is: A diphoton with at least one of the photons not satisfying the photon id MVA threshold and an electron or muon with several cuts flipped. These cuts are, for the muon, a $\Delta R_{\mu\gamma}$ <0.35, and for electrons, a $\Delta R_{\mu\gamma}$ <0.35, and 3.0GeV <$|m_{e\gamma} - m_Z|$ <10.0 GeV. Using this defenition the next step is to make a different control sample for each corresponding diphoton MVA cut. For each data set, the best fit function is chosen using the envelope method (explained in chapter 8). With the chosen background model, and the corresponding singal samples (also with the diphoton mva cut) are used to compute the best fit value for the bosonic signal strength. All events in a category that involves a higgs boson with boson interaction are put in a single poisson distibution. The maximum likelihood fit is found for the distribution, and the signal strenght that maixmizes the likelihood is the result. The value of the diphoton MVA cut that minimizes the uncertainty on this rate is chosen as the optimized value. Due to complications with deadlines and technical strategy, it was found that simply looking at the tagging efficiency as a fucntion of diphoton MVA cut was sufficient enough.

7.2.4 VHHadronictTag

The hadronic tag takes advantage of hadronic decays of the W and Z boson. The invariant mass of the dijet system has to be within a window that cover both the W and Z mass, this reduces the background significantly. To further reduce the background, the fact that the higgs boson recoils against the vector boson implies that the their decay directions will be corrolated. In background no corrolation is expected since a dijet plus diphoton

event in background does not come from a single particle decay. This is reflected by the θ^* variable, which is the angle of between the vector boson in the laboratory frame and the direction of the decay products in the vector boson rest frame.

- p_T^{lead} >0.5
- $p_T^{sublead}$ >0.25
- Diphoton MVA score >0.6
- Photon MVA score >-0.9
- N_{jets} <2
- p_T >40.0 GeV
- Jet $|\eta|$ <2.4
- $\Delta R_{jet\gamma_lead}$ >0.4
- $\Delta R_{jet\gamma_sublead}$ >0.4
- 60.0 GeV $< m_{jetjet} <$120.0 GeV
- $|Cos(\theta^*)|$ <0.5

7.2.5 VHMetTag

This category takes advantage of the Z→$\nu\nu$ decay, and so it is expected to have a high MET value. The category may also pick up events in which none of the main objects were reconstructed properly giving the event a large MET value.

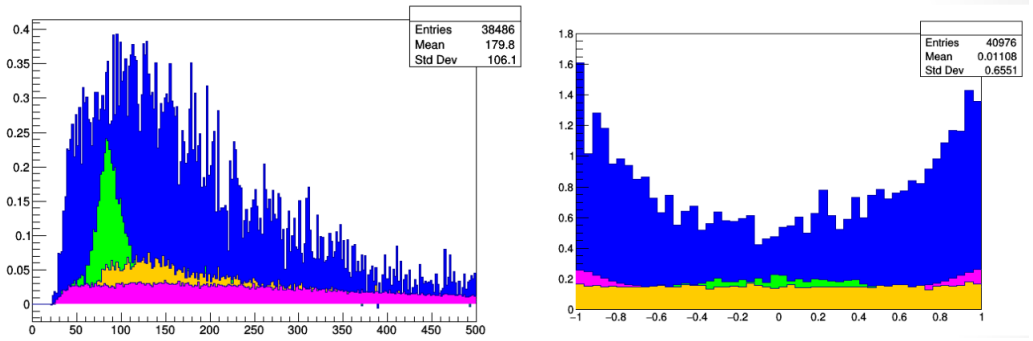

Figure 7.2: The plots are normalized to area, and the x axis have units of GeV. On the left the dijet spectrum is shown for TTH (yellow), GGH (blue), VBF (magenta), and VH (green). On the right the $cos(\theta^*)$ variable is shown. It is clear that GGF provides a significant source of contamination. In general GGH Jets have harder momentum at 13TeV which has led to higher contamination across all jet categories.

- Diphoton MVA score >0.6
- Photon MVA score >-0.9
- $p_T^{lead}/m_{\gamma\gamma}$ >0.375
- $p_T^{sublead}/m_{\gamma\gamma}$ >0.25
- p_T^{MET} >85.0 GeV
- $\Delta\phi_{MET\gamma_\gamma}$ >2.4
- $p_j et$ >50.0 GeV
- Jet $|\eta|$ <2.4
- $\Delta R_{\gamma leadjet}$ >0.5
- $\Delta R_{\gamma subleadjet}$ >0.5

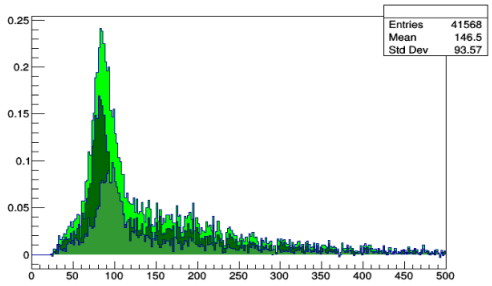

Figure 7.3: WH and ZH conttributions to the VH dijet spectrum, we can see that it would be very hard to untangle the individual contributions of each boson. The z axis are in units of GeV and the y axis are arbitrary units. The plots are normalized by area.

7.3 VBFTag

A BDT is used to discriminate VBF jets from the regular diphoton background and GGF. The kinematics dijet MVA makes use of kinematic variables from the dijet system and diphoton system. There is a preselection imposed on the jets, these are cuts on the jet transeverse momentum of 40 and 30 GeV for the lead and sublead jet respectevely, the invariant mass is also required to be greater than 250 GeV. The variables are:

- $p^{\gamma}{}_{T}^{1}$
- $p^{\gamma}{}_{T}^{2}$
- $p_{T}^{jet1}/m_{\gamma\gamma}$
- $p_{T}^{jet2}/m_{\gamma\gamma}$
- $m_{j}et_{j}et$
- $\Delta\eta_{jet1\,jet2}$

- $\Delta\phi_{j_1 j_2,\gamma\gamma}$
- The centrality variable
- $\Delta\phi_{jj}$
- $\min\Delta(\gamma, jet)$

The centrality variable [4] is defined as: The MVA is trained using the VBF signal samples

$$C_{\gamma\gamma} = \exp\left(-\frac{4}{(\eta_1-\eta_2)^2}\left(\eta_{\gamma\gamma}-\frac{\eta_1+\eta_2}{2}\right)^2\right)$$

and the regular diphoton background with the GGF signal. The combined BDT uses information from the diphoton and dijet system to seperate VBF jets from GGF and background jets. The variables of the VBF MVA are: The kinematics-dijet MVA result, the diphoton mva result and the diphoton transverse momentum. From this discriminant 3 categories are defined based on their signal significance. The cuts are places at VBF Combined MVA >0.957, >0.902, >0.553.

7.4 UntaggedTags

The untagged tags are defined by different cuts in the diphoton MVA distribution. Any envent that does not get classified in any of the GGH,TTH or VBF categories is used for the untagged tags. The categories are defined as : -0.405 <DiphotonMVA <0.204, DiphotonMVA >0.204, >0.564, >0.864.

Chapter 8

Signal Model

8.1 Introduction

Once all the events in data and MC have gone through the event selection, they can now be used for statitical analysis. The main strategy is to make a simple signal model that takes into account all corrections derived throughout the analysis. The signal model in then used for the signal plus background hypothesis later in analysis. The midel is compsed of a sum of gaussians and is done for all mass points. Each model for each mass point is later interpolated to produce a smooth funnction which will represent the signal PDF as a fucntion of $m_{\gamma\gamma}$.

8.2 Signal Model As Function Of $M_{\gamma\gamma}$

First the expected yield for each process is taken into account $\mathcal{L} \times \sigma \times Br \times \alpha \times \epsilon$ correspondingly for each production process. All the corrections are taken into account in

the $\alpha \times \epsilon$ term which also reflect the reduction in events by the event selection criteria. Explicitly there are 4 terms:

- $N_{ggh} = \mathcal{L} \times \sigma_{ggh} \times Br \times \alpha \times \epsilon$
- $N_{vbf} = \mathcal{L} \times \sigma_{vbf} \times Br \times \alpha \times \epsilon$
- $N_{vh} = \mathcal{L} \times \sigma_{vh} \times Br \times \alpha \times \epsilon$
- $N_{tth} = \mathcal{L} \times \sigma_{tth} \times Br \times \alpha \times \epsilon$

for each category, or for each production process there are 16 singal yields corresponding to each category. This brings the total amount of yields to 64 (per mass point). The next step in the signal model (for a single mass point) is to extract the signal shape from the selected events in each category. The signal model function is a Double Crystal Ball (DCB) plus a gaussian. A simultaneous signal fit on all the mass points is done. The singal shapes parameters (DCB plus gaussian parameters) are written as functions of m_H. This gives a continous model for each category as a function of m_H. The right and correct vertex choice are still handled seperately. During this process all the models are normalized to one, once the shapes have been set the normalization is taken care of to take into account all the calculated yields.

$$P^R_{cat0ggh}(m_{\gamma\gamma}|\mu^R_{mH}, \sigma^R_{mH}, DCB^R(\mu), DCB^R(\sigma), \alpha^R_1, \alpha^R_2, n^R_1, n^R_2)$$

$$P^W_{cat0ggh}(m_{\gamma\gamma}|\mu^W_{mH}, \sigma^W_{mH}, DCB^W(\mu), DCB^W(\sigma), \alpha^W_1, \alpha^W_2, n^W_1, n^W_2)$$

$$P_{cat0ggh} = \epsilon P^R_{cat0ggh} + (1-\epsilon) P^W_{cat0ggh}$$

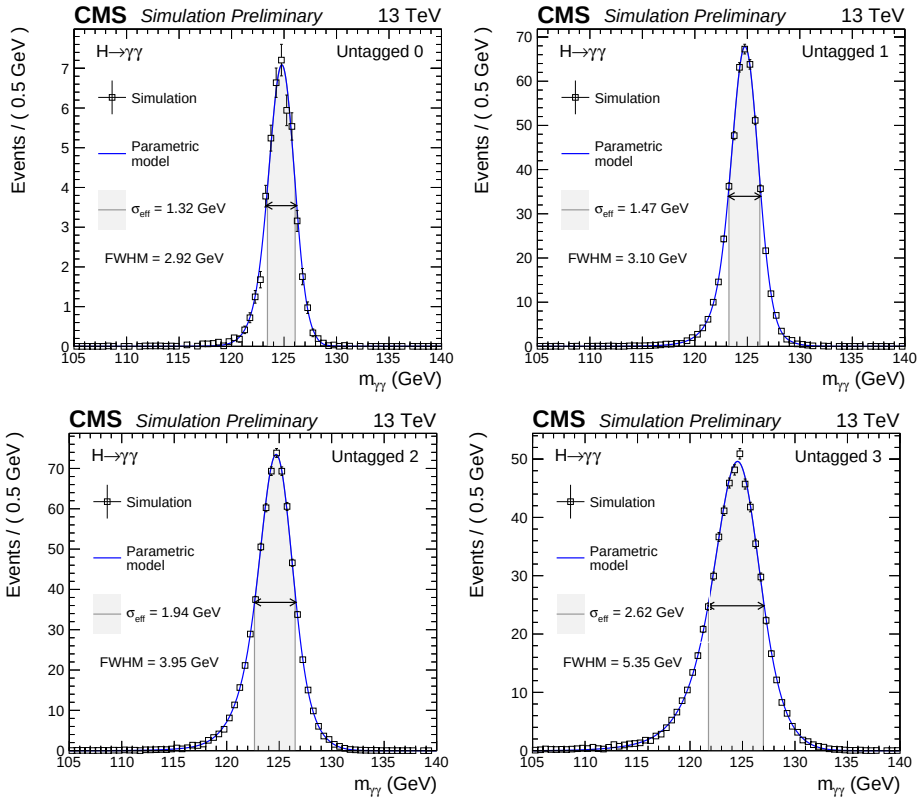

Figure 8.1: Inclusive categories signal model, the highest resolution category of all the analysis un UntaggedTag_0, with a resolution of $\sigma_e ff = 1.32$ GeV.

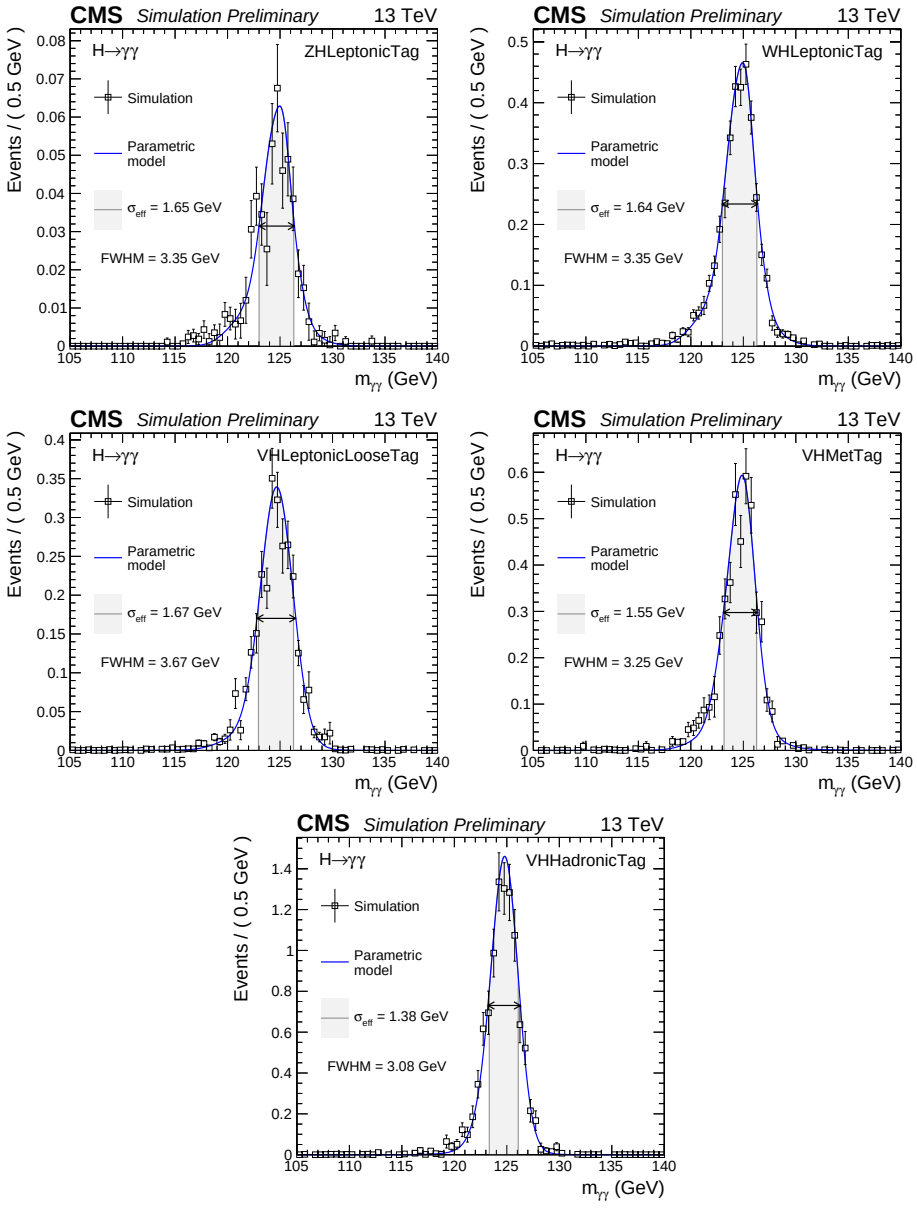

Figure 8.2: Associated production categories signal models, the resolution of VHHadronic is competitive with that of UntaggedTag_0, this is most likely due to the fact that it has a clean dijet topology in its selection

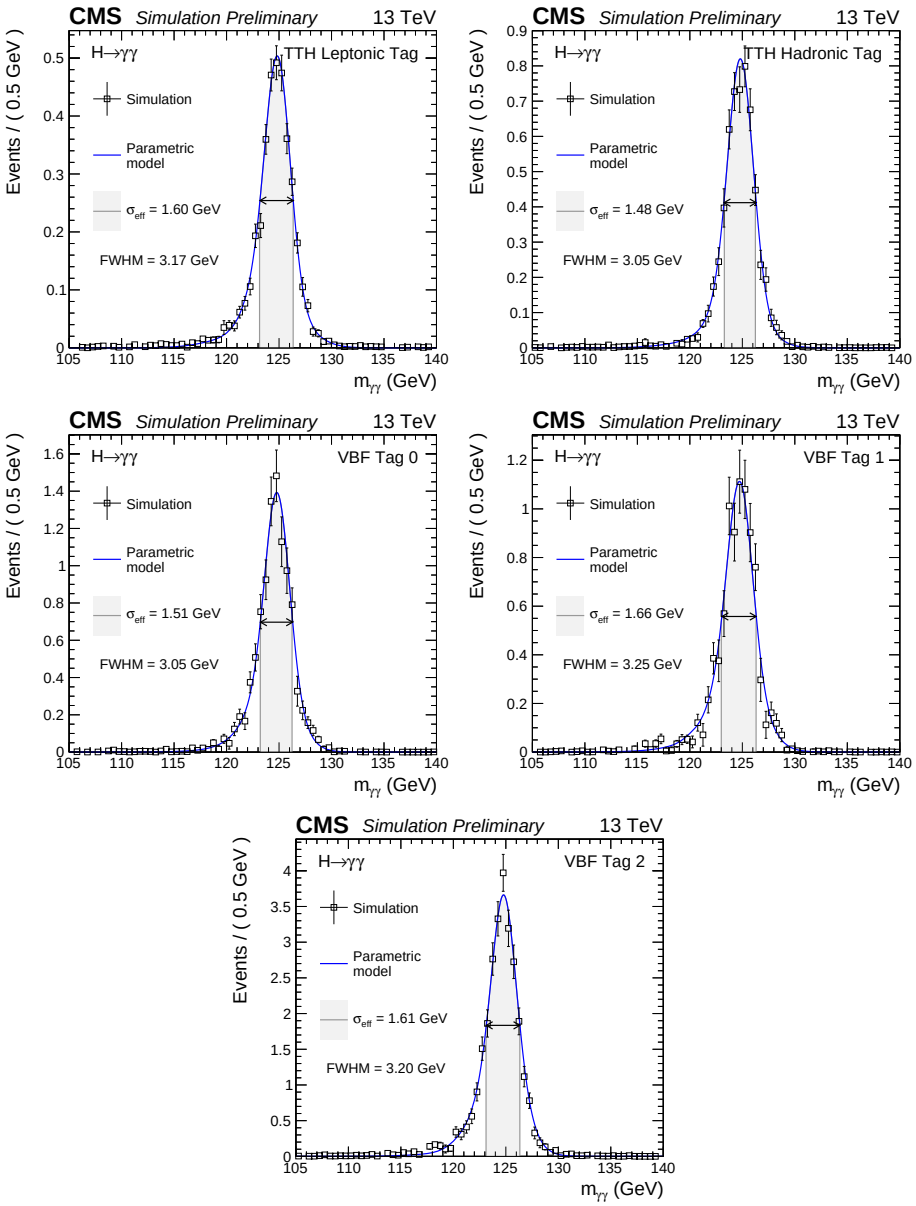

Figure 8.3: Signal model for the VBF process and TTH process

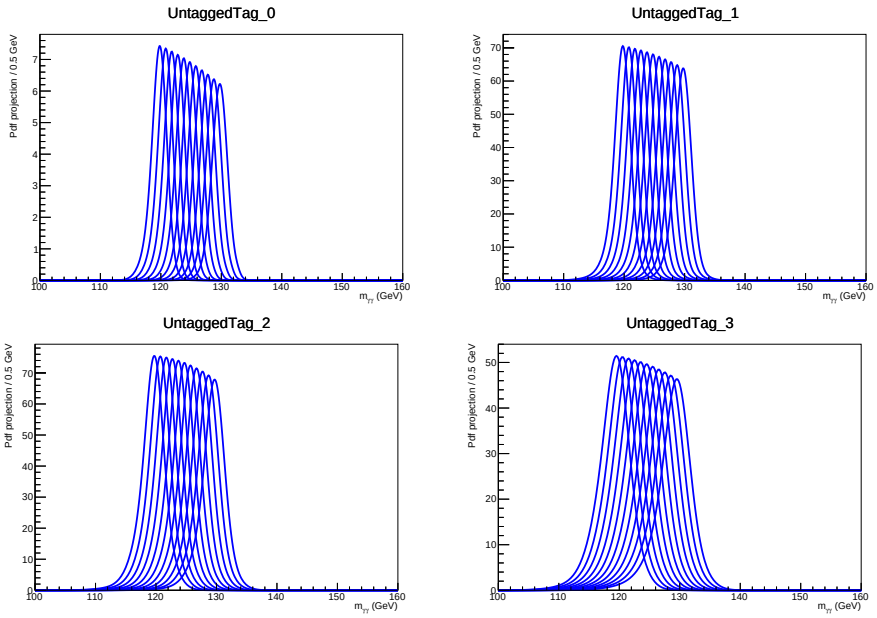

Figure 8.4: Inclusive singal model as a function of mass

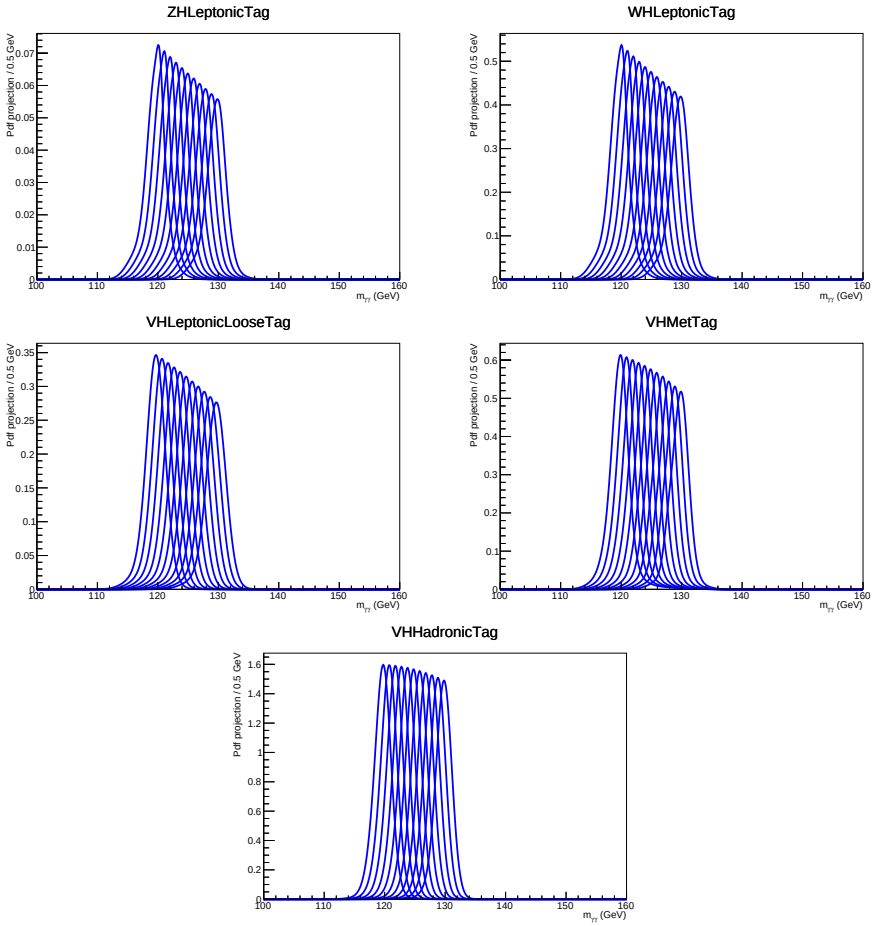

Figure 8.5: Associated production signal models as a function of mass

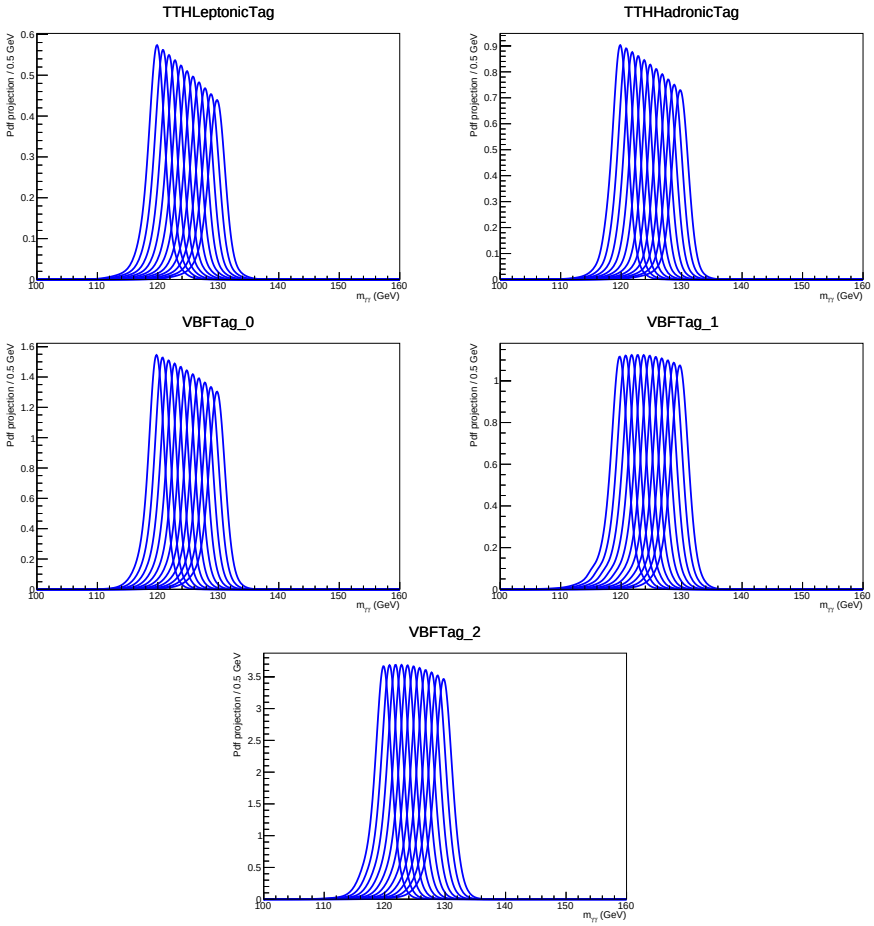

Figure 8.6: VBF and TTH processes signal model as a function of mass

Chapter 9

Background Model

The analysis uses a data driven model for the background. Since the $m_{\gamma\gamma}$ spectrum is smooth and falling, the function shapes used as the background model are not very complicated. To account for the possible uncertainty on choosing the wrong function for the model, the choice of function is used as a nuisance parameter. The implemented method is called The Envelope Method [8]. The sets of functions used are:

- Sums of exponentials:

$$f_N(x) = \sum_i^N p_{2i} e^{p_{2i+1} x}$$

- Sums of polynomials in Bernstein Basis:

$$f_N(x) = \sum_{i=0}^N p_i b_i, b_{(iN)} = \binom{N}{k} x^i (1-x)^(N-i)$$

- Laurent series:

$$f_N(x) = \sum_{i=1}^N p_i x^{-4+\sum_{j=1}^i (-1)^j (j-1)}$$

- Sums of power law functions:

$$f_N(x) = \sum_i^N p_{2i} x^{-p_{2i+1}}$$

The set of functions for each category is limited by a the likelihood ratio test $\frac{\mathcal{L}_{\mathcal{N}}}{\mathcal{L}_{N+1}}$ when p-value >0.1. Once the set of functions has been chosen. This is then used to determine the best fit value of μ_H (the signal strenght), this will be the minimum of the envelope, the uncertainty of this choice of function is taken into account by the width of the envelope.

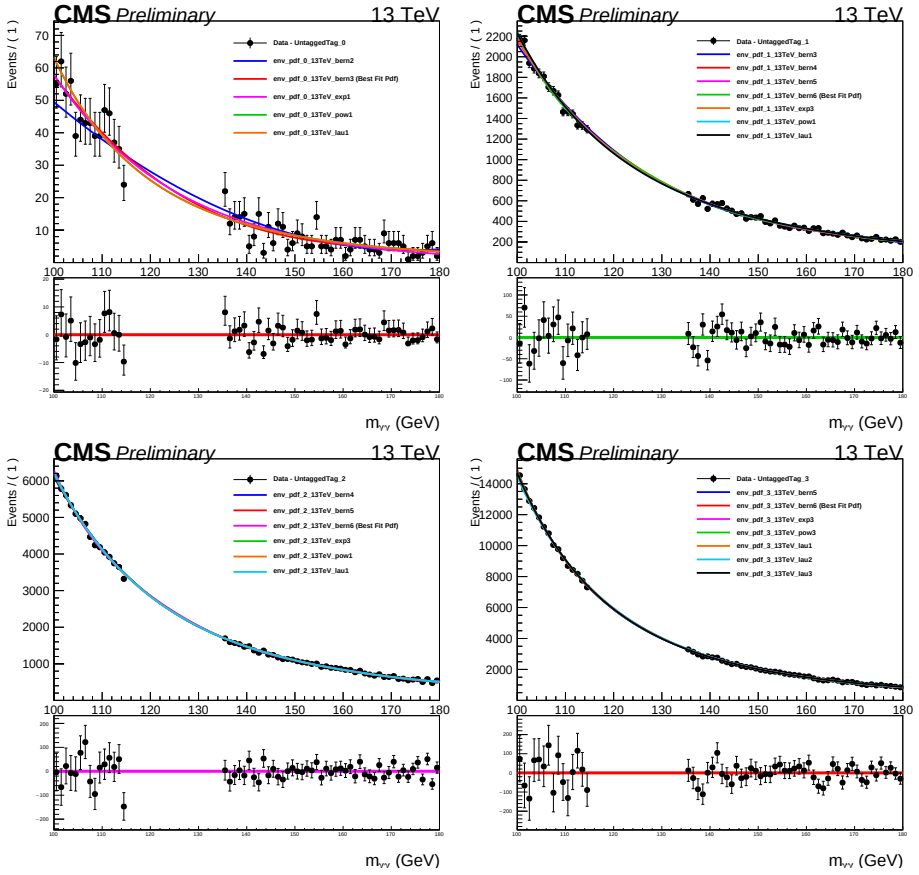

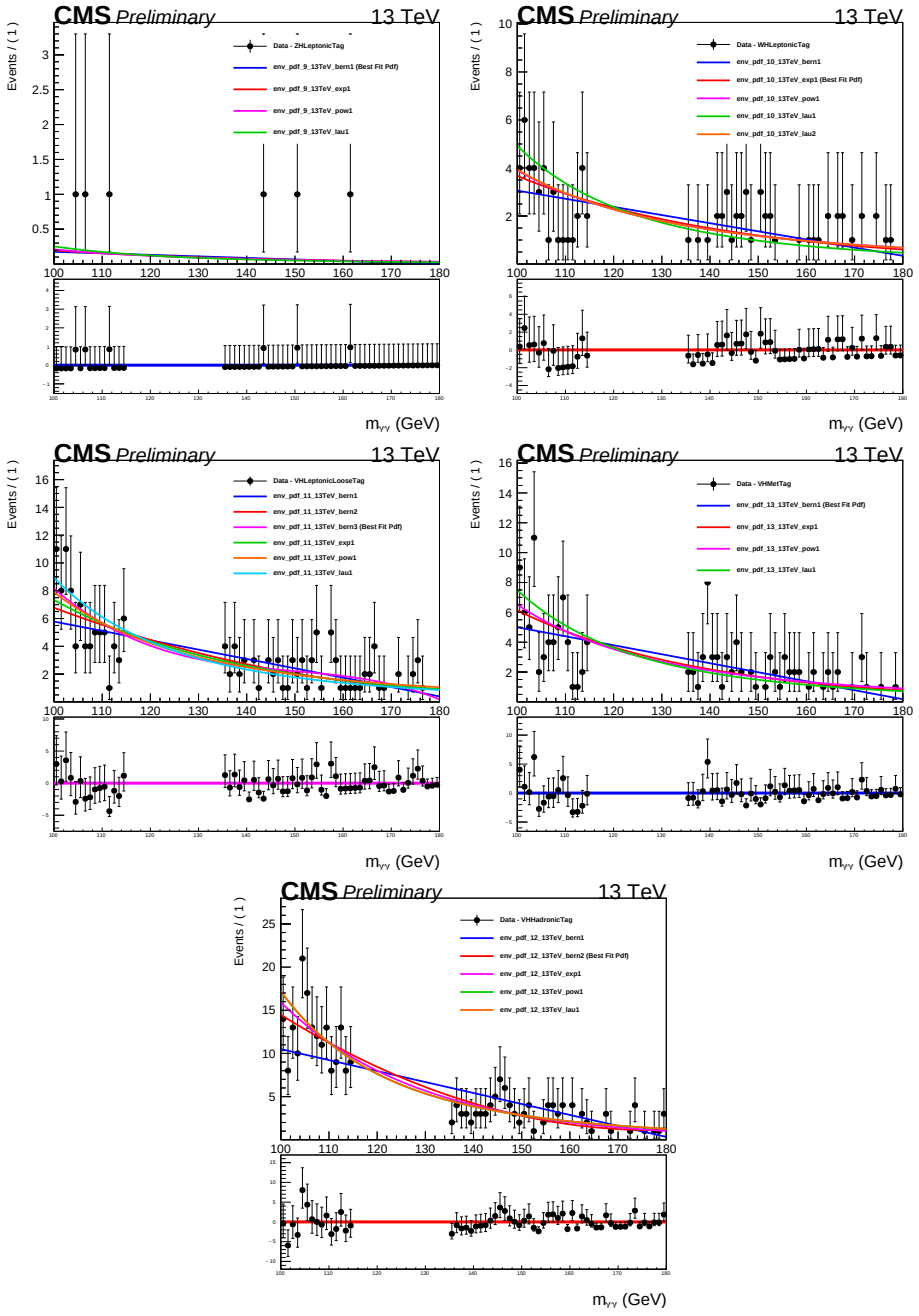

Figure 9.1: Associated production categories signal models, the resolution of VHHadronic is competitive with that of UntaggedTag_0, this is most likely due to the fact that it has a clean dijet topology in its selection

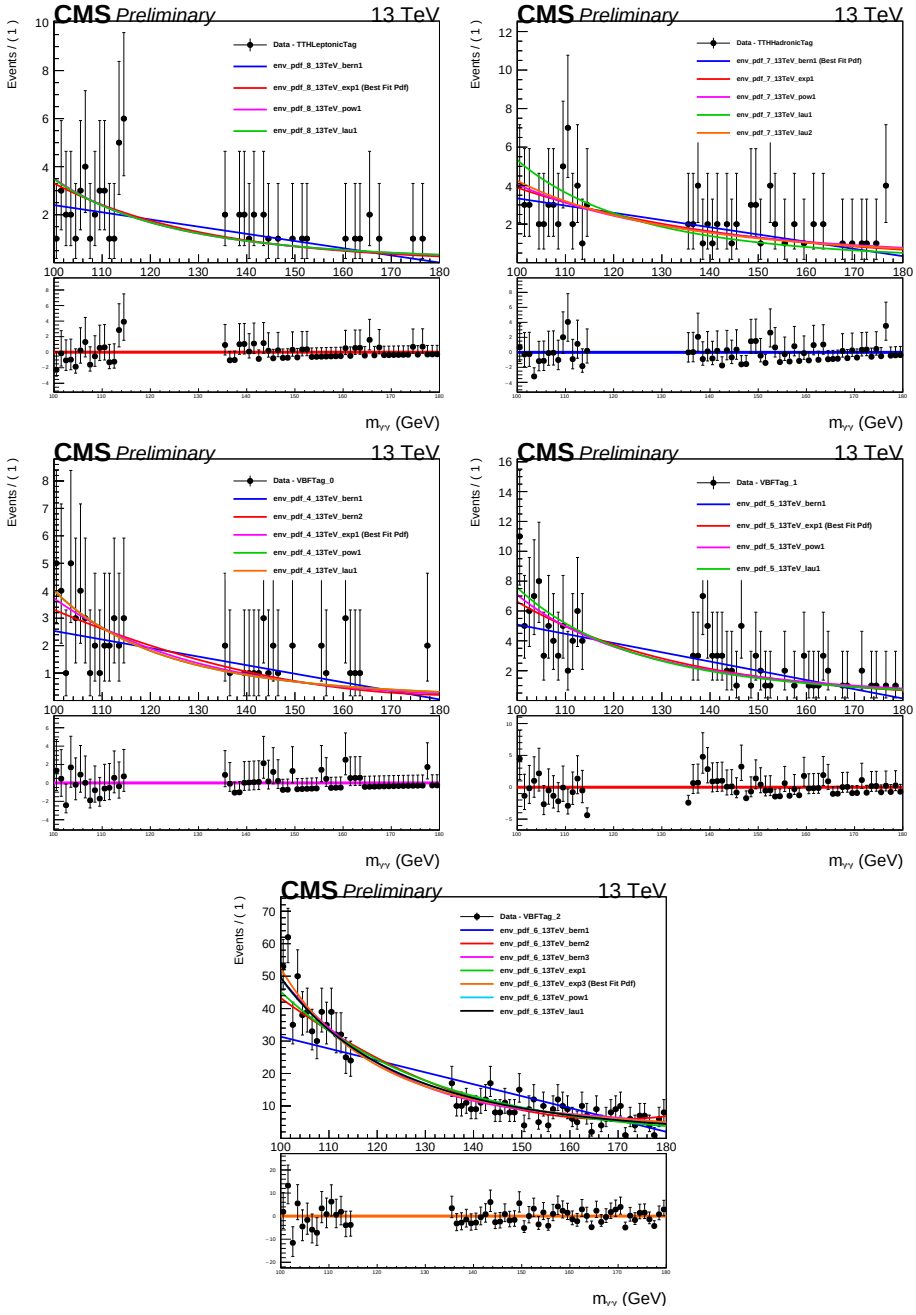

Figure 9.2: Signal model for the VBF process and TTH process

Chapter 10

Systematic Sources

In the analysis there are both theoretical systematics and experimental systematics. Theoretical systematics are due to modeling uncertainties in some physical constants and, for example, the Parton Distribution Functions (PDF) of protons at 13 TeV. These will only affect the signal model since the background model is derived from the data, and the systematic due to function choice is already accounted for in the envelope method. The significance of each systematic is calculated by varying the nominal value of a physical quantity by the value of the uncertainty. This new value (nominal plus uncertainty) is then carried through the rest of the analysis and it's final effect on measured quantities is determined. The systematic uncertainties are:

- PDF: This uncertainty is related to the measured values of PDFs from prvious experiments. These are used as given theoretical values and are used by all analysis that heavily rely on simulations. there are over 100 PDF systematics, their overall effect is on the yield and category migration. The events are re-weighted according to the

PDF4LHC publication.

- α_s: The strong force coupling value. Again the uncertainty comes from previous experiments that measured this value, the re-weighting is handled as is noted in the PDF4LHC publication.

- QCD scale: Uncertainty on the QCD scale.

- Underlying event and parton shower uncertainty: These uncertainties come from the manipulation of MC generators to be able to hadronize a shower or take into account soft collisions (underlying event)

- H$\rightarrow \gamma\gamma$ Branching ratio uncertainty: These is a theoretical uncertainty.

- GGF contamination in TTH and VBF: Due to the mismodeling of GGF in MC, some GGF events can easily match the TTH or VBF selection.

- Integrated luminosity: Uncertainty on the measurement of the integrated luminosity.

- Trigger efficiency: Uncertainty derived from the correction on the data/MC discrepancy in trigger validation.

- Photon pre-selection: Uncertainty derived from the correction on the data/MC discrepancy in the Photon pre-selection.

- Vertex finding efficiency: Uncertainty derived from the correction on the data/MC discrepancy in the Vertex finding efficiency.

- Energy scale and resolution uncertainty: Uncertainty derived from modifications to the R_9 distribution due to elctron-photon differences in MC.

- Photon ID uncertainty: Uncertainty derived from data/MC differences in Z$\rightarrow$ee events.

- Per photon energy resolution estimate uncertainty: Determined by rescaling the resolution.

- Jet energy scale: Modification of the jet energy scale results in intra category migration (within VBF or TTH) and external category migration, mainly to the untagged categories.

- B-tagging efficiency: Derived from data/MC differences in the b-tagging efficiency.

- Lepton identification uncertainty: Derived from data/MC differences in the leptons selection efficiency.

Expected relative uncertainty for SM Higgs boson ($m_{\mathrm{H}} = 125 GeV$)					
Systematic	μ	μ_{ggH}	μ_{qqH}	μ_{VH}	μ_{ttH}
Photon identification	3.40 %	4.59 %	5.39 %	2.05 %	2.77 %
Per photon energy resolution estimate	2.68 %	4.20 %	4.85 %	1.47 %	0.80 %
Trigger efficiency	0.25 %	0.04 %	0.11 %	0.12 %	0.10 %
Diphoton preselection	0.53 %	0.23 %	0.24 %	0.40 %	0.28 %
Electron veto	0.46 %	0.12 %	0.21 %	0.23 %	0.22 %
Vertex finding efficiency	0.56 %	1.22 %	0.28 %	0.52 %	0.42 %
Photon energy scale and smearing	2.55 %	3.02 %	6.62 %	3.21 %	3.19 %
Nonlinearity of detector response	0.40 %	0.27 %	0.26 %	0.33 %	0.15 %
Nonuniformity of light collection	0.31 %	0.20 %	0.03 %	0.16 %	0.26 %
Shower shape corrections	0.44 %	0.36 %	0.14 %	0.55 %	0.27 %
Modelling of material budget	0.25 %	0.08 %	0.12 %	0.13 %	0.29 %
Modelling of detector response in GEANT4	1.17 %	0.32 %	0.11 %	0.17 %	0.08 %
Jet energy scale and resolution	1.70 %	2.53 %	25.82 %	2.09 %	2.17 %
ggF contamination in VBF categories	0.59 %	1.12 %	13.58 %	1.27 %	0.05 %
UE and PS	0.53 %	1.87 %	8.88 %	0.51 %	0.32 %
Lepton reconstruction and btag efficiencies	0.18 %	0.07 %	0.06 %	1.08 %	2.56 %
MET	0.08 %	0.08 %	0.11 %	0.66 %	0.11 %
ggF contamination in ttH categories	0.40 %	0.09 %	0.10 %	0.23 %	5.83 %
Integrated luminosity	2.13 %	2.83 %	5.77 %	3.24 %	2.67 %
Branching ratio	1.65 %	1.96 %	5.12 %	2.69 %	1.97 %
QCD scale yield	2.63 %	4.42 %	0.29 %	1.41 %	10.38 %
PDF and alphaS yield	2.13 %	3.29 %	5.13 %	2.19 %	4.08 %
QCD scale migrations	1.75 %	1.53 %	8.21 %	6.76 %	1.45 %
PDF migrations	0.46 %	0.22 %	0.73 %	0.40 %	0.79 %
AlphaS migrations	0.62 %	0.05 %	1.03 %	0.33 %	0.17 %
Total	7.35 %	10.27 %	34.38 %	9.80 %	14.24 %

Table 10.1: Individual and total effect of the systematics uncertainties on the overall singal strenght, and the per-process signal strength

Chapter 11

$M_{\gamma\gamma}$ Spectra And Results

The following plots are unblinded diphoton invariant mass spectra for 13 TeV proton proton collisions. Each plot is a different category, the chosen background model (function) is shown in red, along with 1 (green) and 2 (yellow) sigma theoretical uncertainty bands, the bottom plot is the spectrum with the background contribution removed. The other results are the likelihood scan for the best fit signal strength, the signal strenght of individual couplings and the p-value of the best fit mass. It has to be noted that due to inconsistencies in the data in early 2017 and an incomplete understanding of all the systematics prevented the collaboration from making a mass measurement this year. The mass valued quoted here does not compete with the mass value measrued for the combined 8 TeV and 7 TeV data set.

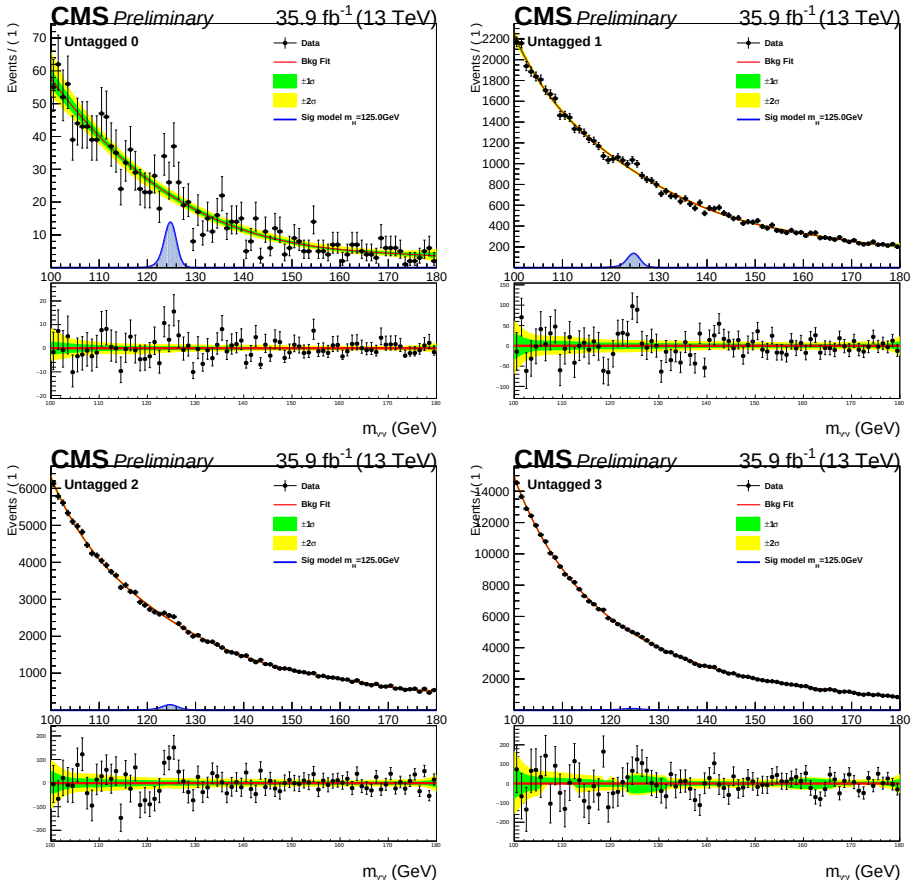

Figure 11.1: $M_{\gamma\gamma}$ spectrum for the untagged categories, it is worth noting the highest populated category is UntaggedTag_3, this category has the highest estimated mass resolution and most signal like diphotons from the rest of the untagged categories.

Event Categories	SM 125GeV Higgs boson expected signal													Bkg (GeV^{-1})	Bkg (GeV^{-1} fb^{-1})	naive expected
	Total	GG2H	VBF	TTH	BBH	THQ	THW	QQ2HLNU	QQ2HLL	WH2HQQ	ZH2HQQ	σ_{eff}	σ_{HM}			
Untagged Tag 0	45.83	80.19 %	11.75 %	1.83 %	0.40 %	0.47 %	0.22 %	0.41 %	0.19 %	2.96 %	1.58 %	1.32	1.24	21.92	0.61	4.10
Untagged Tag 1	480.56	86.81 %	7.73 %	0.56 %	1.15 %	0.13 %	0.02 %	0.47 %	0.27 %	1.81 %	1.04 %	1.47	1.32	924.21	25.74	6.27
Untagged Tag 2	670.45	89.76 %	5.48 %	0.44 %	1.18 %	0.08 %	0.01 %	0.51 %	0.34 %	1.40 %	0.81 %	1.94	1.68	2419.53	67.40	4.71
Untagged Tag 3	610.07	91.13 %	4.51 %	0.48 %	1.07 %	0.07 %	0.01 %	0.55 %	0.30 %	1.21 %	0.69 %	2.62	2.28	4855.00	135.24	2.60
VBF Tag 0	10.01	21.69 %	77.09 %	0.34 %	0.35 %	0.29 %	0.03 %	0.03 %	0.00 %	0.19 %	-0.01 %	1.51	1.30	1.60	0.04	3.09
VBF Tag 1	8.64	33.58 %	64.64 %	0.39 %	0.52 %	0.36 %	0.04 %	0.13 %	0.03 %	0.24 %	0.07 %	1.66	1.38	3.25	0.09	1.79
VBF Tag 2	27.76	50.14 %	46.46 %	0.81 %	0.73 %	0.53 %	0.07 %	0.20 %	0.06 %	0.71 %	0.27 %	1.61	1.36	18.89	0.53	2.42
TTH Hadronic Tag	5.85	10.99 %	0.70 %	77.54 %	2.02 %	4.13 %	2.02 %	0.09 %	0.05 %	0.63 %	1.82 %	1.48	1.30	2.40	0.07	1.49
TTH Leptonic Tag	3.81	1.90 %	0.05 %	87.48 %	0.08 %	4.73 %	3.04 %	1.53 %	1.15 %	0.02 %	0.02 %	1.60	1.35	1.50	0.04	1.18
ZH Leptonic Tag	0.49	0.00 %	0.00 %	2.56 %	0.00 %	0.02 %	0.13 %	0.00 %	97.30 %	0.00 %	0.00 %	1.65	1.43	0.12	0.00	0.53
WH Leptonic Tag	3.61	1.26 %	0.59 %	5.18 %	0.18 %	3.03 %	0.73 %	84.48 %	4.33 %	0.12 %	0.09 %	1.64	1.43	2.09	0.06	0.94
VH LeptonicLoose Tag	2.75	9.16 %	2.70 %	2.34 %	0.57 %	1.81 %	0.13 %	63.62 %	18.87 %	0.56 %	0.23 %	1.67	1.56	3.50	0.10	0.55
VH Hadronic Tag	9.69	57.38 %	3.68 %	3.61 %	0.35 %	1.39 %	0.27 %	0.17 %	0.42 %	20.47 %	12.26 %	1.38	1.31	7.22	0.20	1.48
VH Met Tag	4.25	23.63 %	2.46 %	14.45 %	0.41 %	2.00 %	1.14 %	25.17 %	28.60 %	1.32 %	0.82 %	1.55	1.38	3.49	0.10	0.88
Total	1883.77	86.96 %	7.09 %	1.00 %	1.09 %	0.15 %	0.04 %	0.81 %	0.42 %	1.55 %	0.89 %	1.95	1.62	8264.73	230.22	10.57

Table 11.1: Signal and background yiedls in all categories for different higgs production processes

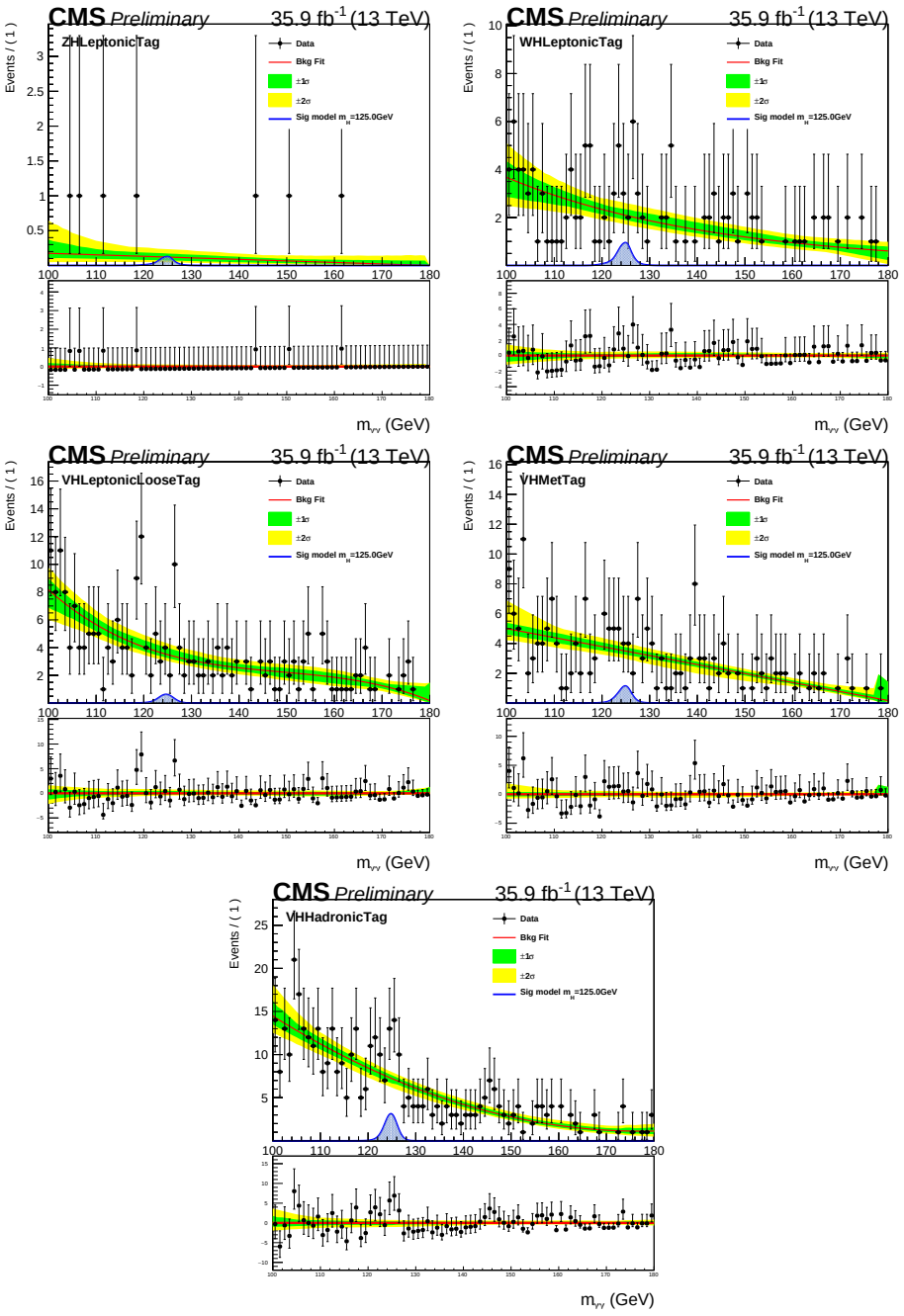

Figure 11.2: $M_{\gamma\gamma}$ spectrum for the associated production categories.

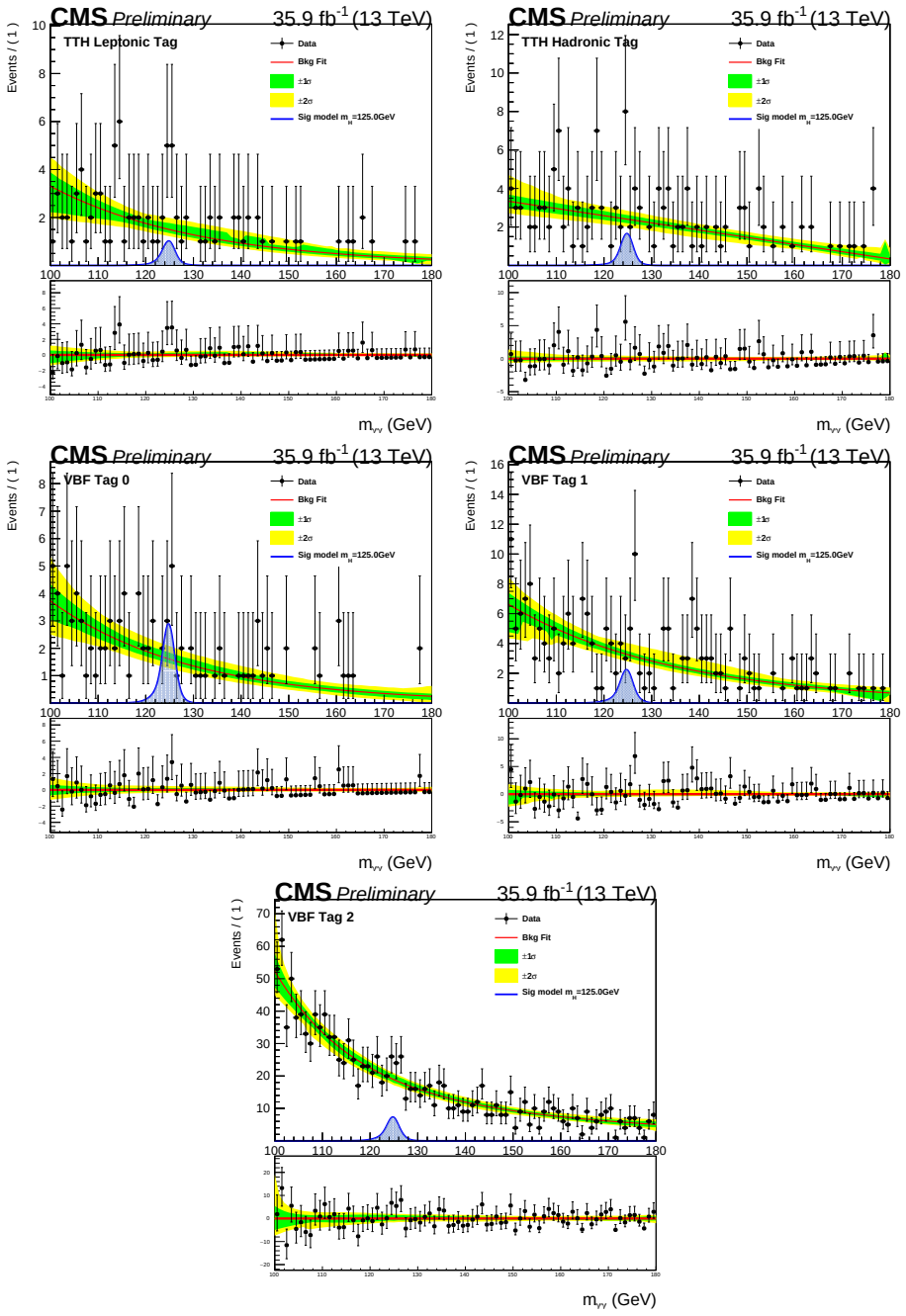

Figure 11.3: $M_{\gamma\gamma}$ spectra for VBF and TTH categories.

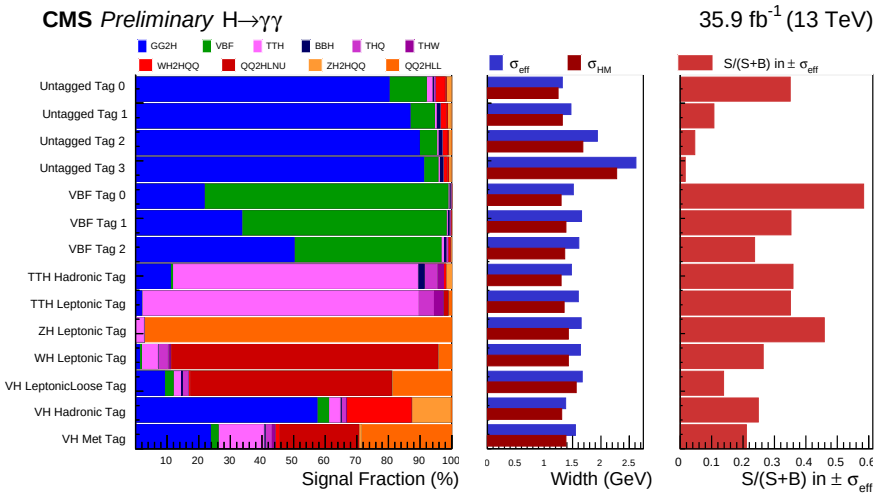

(a)

Figure 11.4: Per process signal yields as a percentage in each category

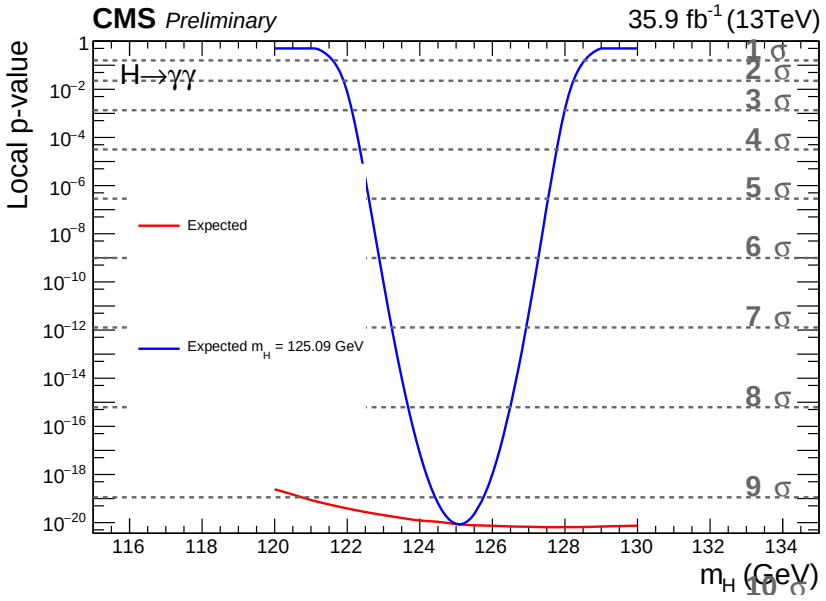

Figure 11.5: p value scan over the higgs mass. The best fit value is at a mass of 125.09 GeV with a significance of $\sim 9.3\sigma$

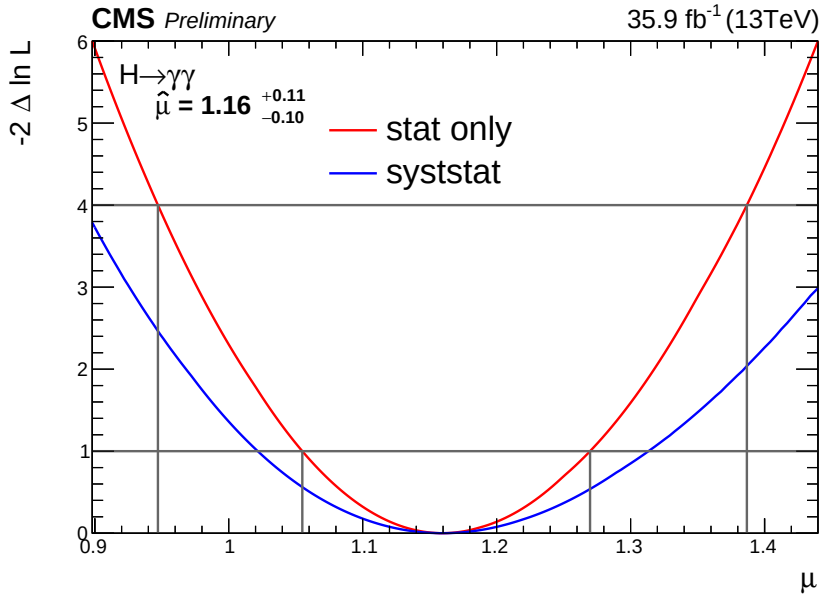

Figure 11.6: signal strength scan with higgs boson mass profiles

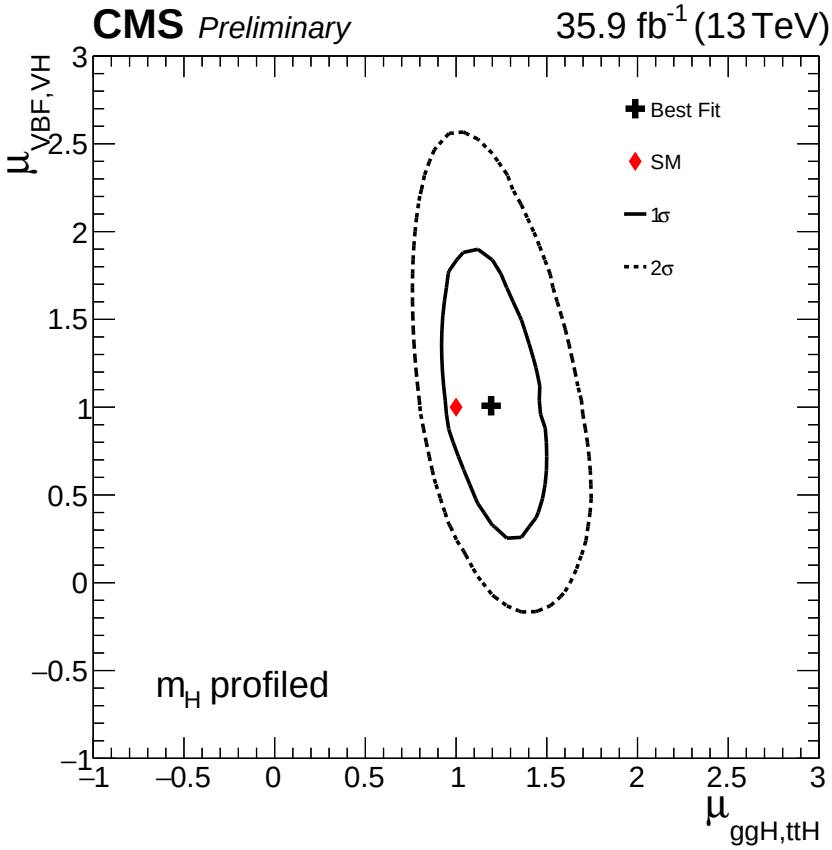

Figure 11.7: Modified coupling 2D fit, the best fit coupling to fermions simultaneously being fitted with the best fit coupling to bosons.

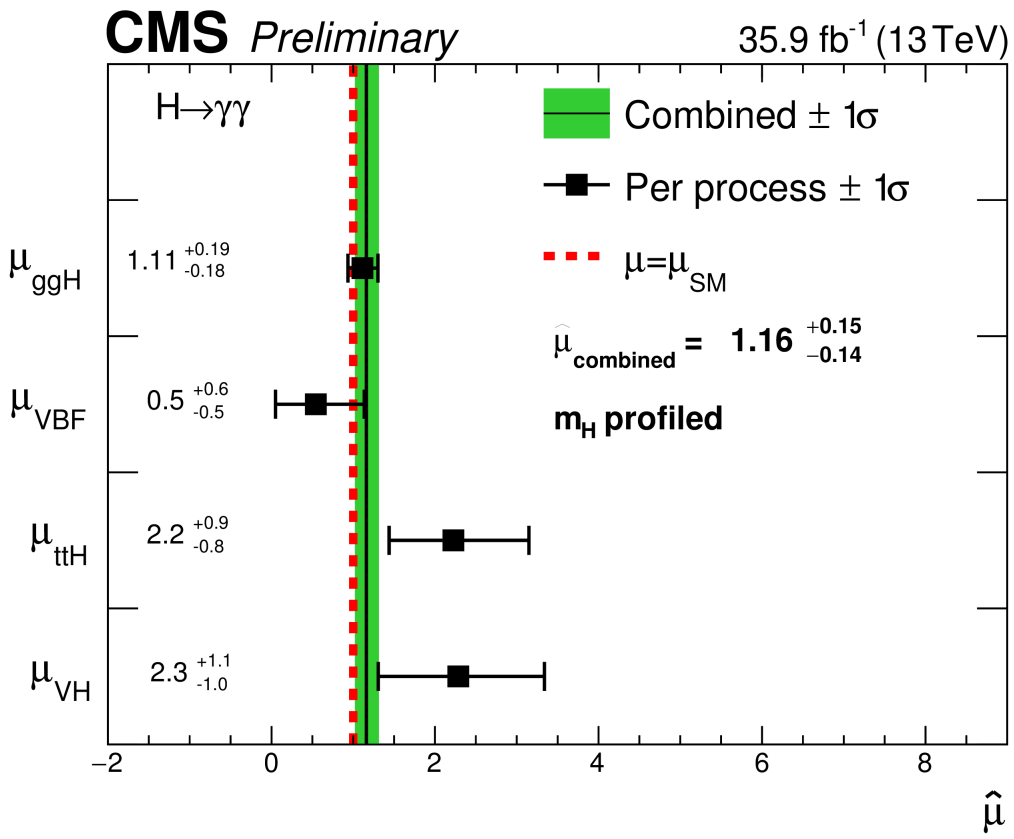

Figure 11.8: Per production process signal strength

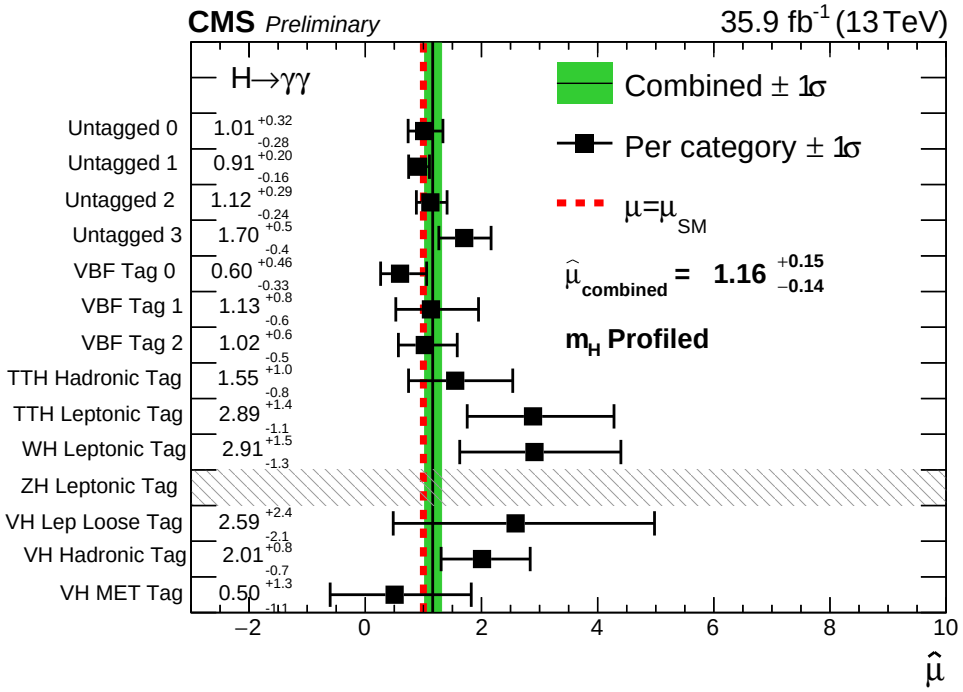

Figure 11.9: Per category signal strength, there were no events in the ZHLeptonicTag so the bin was grayed out

Chapter 12

Conclusion And Prospects

The measured signal strength ($\sigma_{obs}/\sigma_{theo}$) is $1.16^{+0.11}_{-0.10}$, the best fit mass is $m_H = 125.09$ GeV at a significance of 9.3σ, and both the measured fermionic coupling and bosonic coupling lie within 1σ of the SM value. These properties fall in line with the SM predictions and there is no sign of inconcistencies.

Prospects for the analysis include: the addition of new production channels (the custom software allows for easy adddition), the collection of more data to reduce the statistical error, and the application of new analysis techniques that could improve the presicion of the analysis.

Bibliography

[1] Kirk Arndt et al. Silicon sensors development for the CMS pixel system. *Nuclear Instruments & Methods in Physics Research*, 2013.

[2] Gino Bolla et al. Design and test of pixel sensors for the CMS experiment. *Nuclear Instruments & Methods in Physics Research*, 2001.

[3] ATLAS Collaboration. Observation of a new particle in the search for the Standard Model Higgs boson with the ATLAS dectector at the LHC. *Phys.Lett.*, 2012.

[4] ATLAS Collaboration. Evidence for Higgs Boson Decays to the $\tau^+\tau$ Final State with the ATLAS Detector. *inSPIRE*, 2013.

[5] CMS Collaboration. The CERN Large Hadron Collider: Accelerator and Experiments, vol 1. *JINST*, 2009.

[6] CMS Collaboration. Observation of a new boson at a mass of 125 gev with the CMS experiment at the LHC. *Phys.Lett.*, 2012.

[7] LHC Higgs Cross Section Working Group Collaboration. Handbook of LHC Higgs Cross Section: 4. Deciphering the Nature of the Higgs Sector. *arXiv.1610.07922*, 2016.

[8] P. Dauncey et al. Handling uncertainties in background shapes: the discrete profiling method. *JINST*, 2015.

[9] Meschi Emilio et al. Electron reconstruction in the CMS Electromagnetic Calorimeter. *CMS-NOTE-2001-034*, 2001.

[10] Andrea Massironi. Precision electromagnetic calorimetry at the energy frontier: CMS ECAl at LHC Run 2. *arXiv.1510.02745v1*, 2015.

[11] Lewis H. Ryder. *Quantum Field Theory*. PRESS SYNDICATE OF THE UNIVERSITY OF CAMBRIDGE, 1996.